Journal of
*Manufacturing and
Materials Processing*

Review

Negative Thermal Expansion Metamaterials: A Review of Design, Fabrication, and Applications

Devashish Dubey *, Anooshe Sadat Mirhakimi and Mohamed A. Elbestawi *

Department of Mechanical Engineering, McMaster University, Hamilton, ON L8S 4L7, Canada; mirhakia@mcmaster.ca
* Correspondence: dubeyd@mcmaster.ca (D.D.); elbestaw@mcmaster.ca (M.A.E.)

Abstract: Most materials conventionally found in nature expand with an increase in temperature. In actual systems and assemblies like precision instruments, this can cause thermal distortions which can be difficult to handle. Materials with a tendency to shrink with an increase in temperature can be used alongside conventional materials to restrict the overall dimensional change of structures. Such structures, also called negative-thermal-expansion materials, could be crucial in applications like electronics, biomedicine, aerospace components, etc., which undergo high changes in temperature. This can be achieved using mechanically engineered materials, also called negative thermal expansion (NTE) mechanical metamaterials. Mechanical metamaterials are mechanically architected materials with novel properties that are rare in naturally occurring materials. NTE metamaterials utilize their artificially engineered architecture to attain the rare property of negative thermal expansion. The emergence of additive manufacturing has enabled the feasible production of their intricate architectures. Industrial processes such as laser powder bed fusion and direct energy deposition, both utilized in metal additive manufacturing, have proven successful in creating complex structures like lattice formations and multimaterial components in the industrial sector, rendering them suitable for manufacturing NTE structures. Nevertheless, this review examines a range of fabrication methods, encompassing both additive and traditional techniques, and explores the diverse materials used in the process. Despite NTE metamaterials being a prominent field of research, a comprehensive review of these architected materials is missing in the literature. This article aims to bridge this gap by providing a state-of-the-art review of these metamaterials, encompassing their design, fabrication, and cutting-edge applications.

Keywords: mechanical metamaterials; multimaterial 3D printing; additive manufacturing; laser powder bed fusion; direct energy deposition

check for updates

Citation: Dubey, D.; Mirhakimi, A.S.; Elbestawi, M.A. Negative Thermal Expansion Metamaterials: A Review of Design, Fabrication, and Applications. *J. Manuf. Mater. Process.* **2024**, *8*, 40. https://doi.org/10.3390/jmmp8010040

Academic Editors: Mohammad J. Mirzaali and Amir A. Zadpoor

Received: 4 January 2024
Revised: 5 February 2024
Accepted: 12 February 2024
Published: 14 February 2024

Copyright: © 2024 by the authors. Licensee MDPI, Basel, Switzerland. This article is an open access article distributed under the terms and conditions of the Creative Commons Attribution (CC BY) license (https://creativecommons.org/licenses/by/4.0/).

1. Introduction

The control of thermal expansion is a critical requirement in present-day industrial applications. A strain change as small as 10^{-5} in linear distortion has the potential to cause fatal errors in high-precision machines and their components [1]. This is evident in the creation of cutting-edge contemporary sectors, such as semiconductor manufacturing, fuel cell technology, thermoelectric converters, electronic packaging, and so forth [2,3]. The fundamental technology used to regulate thermal expansion involves materials that exhibit negative thermal expansion (NTE) which shrink when heated [2,4–6]. Research on negative thermal expansion garnered significant interest after the discovery of isotropic NTE in ZrW_2O_8 in 1996 [7]. Later, several different compounds were found to exhibit NTE behavior in various temperature ranges [8–11]. The NTE behavior found in these materials was caused by the molecular level structure of the constituent compounds in their NTE temperature range. As such, it is also very difficult to find these rare materials in nature, and a substantial amount of effort is required to discover them. Nonetheless, in 1996, Lakes et al. discovered a novel method of producing negative thermal expansion behavior primarily using structural architecture instead of material properties [12]. He designed an NTE strip by attaching two different materials with different positive coefficients of thermal expansion [12]. Due to its highly material-independent approach, this work spurred remarkable progress in the field of mechanically engineered negative-thermal-expansion materials also called "negative thermal expansion mechanical metamaterials" [13–35]. A metamaterial (deriving from the Greek word μετά (meta), meaning "beyond" and the Latin word materia, meaning "matter") is a material engineered to have a property rarely found in natural materials. Mechanical metamaterials are metamaterials with engineered architectures that exhibit exotic properties, primarily governed by their structure rather than their composition. The primary exotic property is thermal expansion in NTE metamaterials. These metamaterials have the potential to achieve the same effect as those produced by rare, naturally available NTE materials. In this article, we will discuss the state-of-the-art design of their architectures, the potential to fabricate them using metal additive manufacturing techniques, and their applications. Hence, the article layout is as follows. First, a comprehensive review of different NTE architectures is discussed. Afterwards, two cutting-edge metal additive manufacturing processes, powder bed fusion (PBF) and direct energy deposition (DED), are reviewed to evaluate their potential to fabricate metal-based NTE metamaterials. Finally, we list excellent current and potential applications of NTE metamaterials to gauge their transformative potential.

2. Design

Since the advent of NTE metamaterials by Lakes et al. in the 1990s, several designs and structures have been proposed for achieving negative thermal expansion. Although they differ in structural designs, the main principle involves joining two or more constituents with different coefficients of thermal expansion (CTE) to generate a structure with an overall NTE. In this section, we have classified and reviewed different design methodologies from the literature so far. Based on the mechanics and failure modes of these architectures, they can primarily be categorized as bending-based or stretch-based with many sub-classifications.

2.1. Bending-Based Architectures

These types of NTE designs work based on the principle of bending. Bending caused in the structure due to the differential expansion of two different bonded materials leads to an overall contraction in one or more directions. These structural designs can be further classified into the following:

1. Bimaterial-strip-based designs;
2. Chirality-based designs;
3. Re-entrant designs;
4. Other designs.

2.1.1. Bimaterial-Strip-Based Designs

In 1996, Lakes et al. [12] proposed a novel method for producing a cellular NTE structure using bimaterial strips. The strips were made from two materials with different CTE values. During an increase in temperature, a differential strain produced at the perfectly bonded interface produces curvature in the strip, which brings the endpoints closer to each other, thereby causing a contraction and leading to an overall negative CTE.

The CTE of the bimaterial strip is given by [12] as follows:

$$\alpha = \frac{l_{arc}}{(h_1 + h_2)} \times \frac{6(\alpha_2 - \alpha_1)\left(1 + \frac{h_1}{h_2}\right)^2}{3\left(1 + \frac{h_1}{h_2}\right)^2 + \left(1 + \frac{h_1 E_1}{h_2 E_2}\right)\left(\left(\frac{h_1}{h_2}\right)^2 + \frac{h_2 E_2}{h_1 E_1}\right)} \times \left[\frac{1}{2}\cot\left(\frac{\theta}{2}\right) - \frac{1}{\theta}\right]$$

where layers E_1 and E_2 denote Young's moduli, α_1 and α_2 are the CTE values of the two materials, θ is the initial curvature of the strip, and h_1 and h_2 denote the thicknesses of strips 1 and 2. If the high-expansion material is placed on the convex side with a slow expanding material on the concave side, a temperature increase will lead to the increased curvature of the strip and negative thermal expansion. The magnitude of the CTE is highly dependent on the ratio of the length of the strip to its thickness, which implies that slender strips have higher magnitudes of expansion, which are negative or positive depending on constituent orientation.

In later works, Lakes and his group suggested the use of these bimaterial strips as edges of two-dimensional and tridimensional lattices with pin joints and analytically achieved negative thermal expansion in these units [13,14]. The curvature of these structures was deliberately minimized to enhance their stiffness. Nevertheless, as their functionality relies on bending induced by the differential expansion of the ribs, we categorize them as architectures primarily governed by bending. Based on the triangular 2D design proposed by Lehman and Lakes, Ha et al. assumed bonded joints (instead of pin joints) as they are more practical and used a finite element analysis to conclude that the structure still showed tuneable thermal expansion characteristics with possible overall negative CTE [36].

Along with bimaterial strips, layers of multiple materials have also been used to achieve anisotropic negative thermal expansion. A pioneering work by Grima et al. [19] describes the use of thick layers of materials with low moduli and CTE values and a high Poisson's ratio combined with thin layers of materials with high moduli and CTE values and a significantly lower Poisson's ratio.

2.1.2. Chirality-Based Designs

In a novel work, Ha et al. alternately oriented bimaterial strips as edges in a chiral structure and achieved negative expansion properties [16]. The expression is given as follows:

$$\alpha = \frac{r}{4\rho_{\mathrm{s}}} \frac{1}{\sqrt{1 + \left(\frac{2r}{L_{\mathrm{rib}}}\right)^2}}$$

where ρ_s is the specific curvature.

Wu et al. also used bimaterial strips in anti-chiral structures to achieve this objective [20]. He ran simulations as well as experiments for his anti-trichiral and anti-tetrachiral bidimensional (2D) designs and then extended his work to tridimensional (3D) structures. The extent of the negativity of overall CTE in his designs was dependent on the node radii, the difference in the thermal expansion of the component materials, and the length of the joining ligaments between the nodes.

2.1.3. Re-Entrant Designs

A re-entrant structure is derived from a honeycomb structure by directing two opposite vertices of its hexagon inwards. Taking inspiration from the use of re-entrant structures in the field of auxeticity, Ai et al. proposed a re-entrant unit cell-based structure with several designs using two different materials and achieved negative thermal expansion along with a negative Poisson's ratio in their simulations [26]. Such structures are termed doubly negative structures. In another work, they made several 3D structures also based on the 2D re-entrant design as it was found to be most optimal in terms of achieving both NTE and auxeticity [25]. Later, Raminhos et al. fabricated a 2D re-entrant NTE design using the additive manufacturing of polymers and experimentally verified its properties [27]. Recently, Peng et al. developed novel hybrid honeycomb designs with enhanced stiffness and tuneable thermal expansion as well as auxeticity [35]. For 2D structures, they merged hexagonal honeycomb unit cells and produced re-entrant, semi-re-entrant, and non-re-entrant designs. In another work, they orthogonally assembled and merged these planar designs to generate 3D unit cells [34].

2.1.4. Other Designs

There are a few bending-dominated structural designs proposed in the literature that do not fit into the above sub-classifications. For instance, Jefferson et al. proposed a hexagonal grid with inner elements made of a higher-CTE material to achieve a bending-based negative CTE design. They analytically evaluated its performance with different beam element-based models and predicted overall negative thermal expansion properties for the structure [24]. Another design proposed by Lim et al. was also found in the literature, exhibiting tuneable thermal expansion characteristics [37]. Figures 1 and 2 depict the 2D and 3D architectures of various designs discussed in this section respectively.

2.2. Stretch-Based Architectures

The structures based on bimaterial strips tend to be less stiff at higher temperatures due to bending, which is a necessity for NTE performance. Avoiding bending-dependent NTE unit cells can increase the overall strength and stiffness of the resultant structure. For designs without bimaterial struts, Deshpande et al. provided a criterion for stretch-based architectures which requires a minimum node connectivity of six for 2D structures and twelve for 3D ones [38]. A design that has a combination of nodes satisfying and not satisfying this criterion would lead to a stiffness lower than a fully stretch-based design; however, the resultant structure can still be stretch-dominated. The stretch-dominated designs made for negative CTE can be classified as follows:

5. Triangle-based;
6. Tetrahedron-based;
7. Octahedron-based;
8. Other designs.

2.2.1. Triangle-Based

Grima et al. proposed a triangular 2D grid with tuneable thermal expansion capable of achieving negative CTE. Unlike strips or layers, this structure only required vertex–vertex contact of edges made of dissimilar materials [17]. Steeves et al. also proposed pin-jointed stretch-dominated designs using triangles that do not undergo bending at higher temperatures and thus have much higher stiffness and thermal fatigue-resistant properties [21] (Figure 1).

Wei et al. took a similar approach with biomaterial-triangle-based designs and proposed various structural shapes for applications [22]. They also fabricated and assembled their designs using various metals and alloys with a high CTE difference, like aluminium and invar, and experimentally investigated the CTE along with stiffness. Li et al. introduced a Hoberman-circle-based NTE system [23]. By attaching radially aligned high-thermal-expansion rods in the middle-to-low-thermal-expansion rods of the Hoberman sphere, the overall structure exhibits negative thermal expansion. Upon heating, the central rods experience a greater amount of expansion than the rods of the Hoberman circle, thereby causing a contraction.

2.2.2. Tetrahedron-Based

In a pioneering work, Lim and coworkers introduced an NTE design using tetrahedrons. By carefully making the base of the tetrahedron with materials with higher CTE values and the rest with lower-CTE material, the tetrahedron exhibits negative CTE in the vertical direction as well as an overall negative volumetric CTE in various cases [29]. Their work led to further research by Xu et al. in the domain of tetrahedron-based NTE designs. They designed various lattice structures based on bimaterial tetrahedrons, particularly thermally negative octet lattice designs [31].

2.2.3. Octahedron-Based

Jin et al. presented a micro-lattice design with a cubic unit cell consisting of twelve quarter-octahedra at the edges. With the material type differing between the octahedral edges and cubic edges, the structure performed well analytically, with promising negative and zero CTE values [32]. In one of their works, Xu et al. utilized octet truss-based architectures to come up with multiple highly tuneable stretch-based designs. Both numerical as well as experimental methods were used to assess the CTE performance of the designs with Al6061 (high CTE) and Ti6Al4V (low CTE) as the constituents, and the structures were manufactured via the snap-fit assembly of metal sheets cut using a laser from the two materials [30].

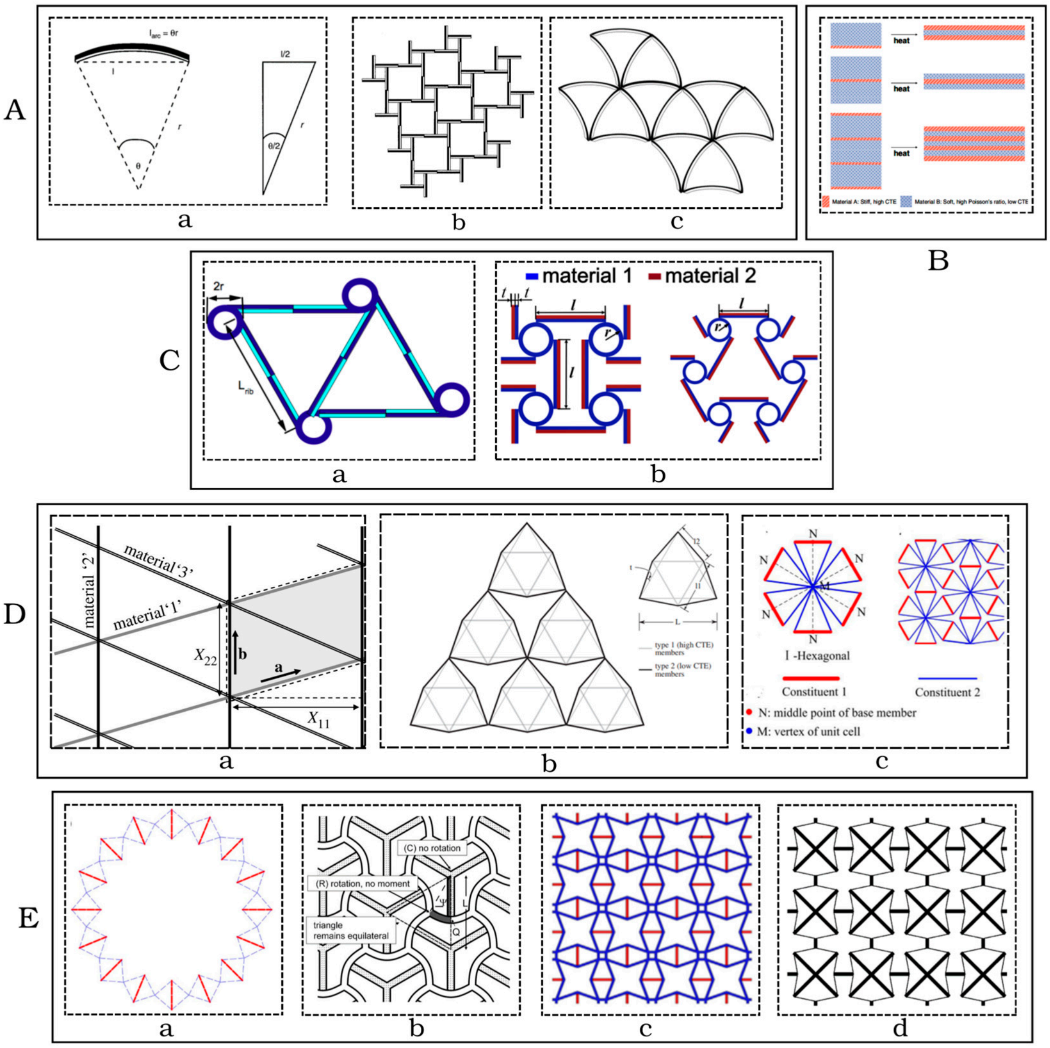

Figure 1. 2D NTE metamaterials: (**A**) Bimaterial-strip-based: (a) Concept of bimaterial strip (Reprinted with permission from [12]; Copyright 1996 Springer Nature), (b) Cellular structure of bimaterial strips (Reprinted with permission from [12]; Copyright Springer Nature), and (c) Equilateral triangular lattice using curved bimaterial ribs [14]. (**B**) Multilayered strip with vertical NTE (Reprinted with permission from [19]; Copyright 2010 John Wiley and Sons.). (**C**) Chirality-based: (a) Chiral lattice with bimaterial strip ligaments where lighter blue and darker blue represent two different constituents (Reprinted with permission from [16]; Copyright 2015 John Wiley and sons), and (b) Bimaterial anti-tetrachiral and anti-trichiral lattice units (Reprinted with permission from [20]; Copyright 2016 American Chemical Society). (**D**) Stretch-based: (a) Triangular grid design (Reprinted with permission from [17]; Copyright 2007 The Royal Society (U.K.)), (b) Triangle lattice NTE (Reprinted with permission from [21]; Copyright 2007 Elsevier), and (c) Hexagonal lattice design (Reprinted with permission from [22]; Copyright 2016 Elsevier). (**E**) Others NTE designs: (a) Hoberman-circle-inspired design where red colour represents the constituent with larger CTE while blue represents constituent with lower CTE (Reprinted with permission from [23]; Copyright 2018 Elsevier), (b) Hexagonal grid design (Reprinted with permission from [24]; Copyright 2009 Elsevier), (c) Re-entrant structure where red colour represents the constituent with larger CTE while blue represents constituent with lower CTE (Reprinted with permission from [26]; Copyright 2017 Elsevier), and (d) X-shaped structure (Reprinted with permission from [37]; Copyright 2005 Springer Nature).

2.3. Other Designs

This section includes architectures that cannot be particularly classified as bending- or stretch-based. In a related work, Lim et al. proposed ring rod assembly-based structures [28]. The unit cell of the design consists of a ring with two rods attached diametrically opposite to each other with each rod protruding out through a hole in the ring on the opposite side. Starting from a 2D structure, they developed 3D arrays of double rings as well. In addition to having thermally negative coefficients, his designs also showed auxetic behavior. Juasiripukdee et al. designed a tessellated cellular structure for a controlled thermal expansion frame for high-precision instruments. They used a high-expansion cylindrical part fitted inside an outer lattice part and numerically confirmed their results [33]. This is an example of a real-world use of controlled thermal expansion.

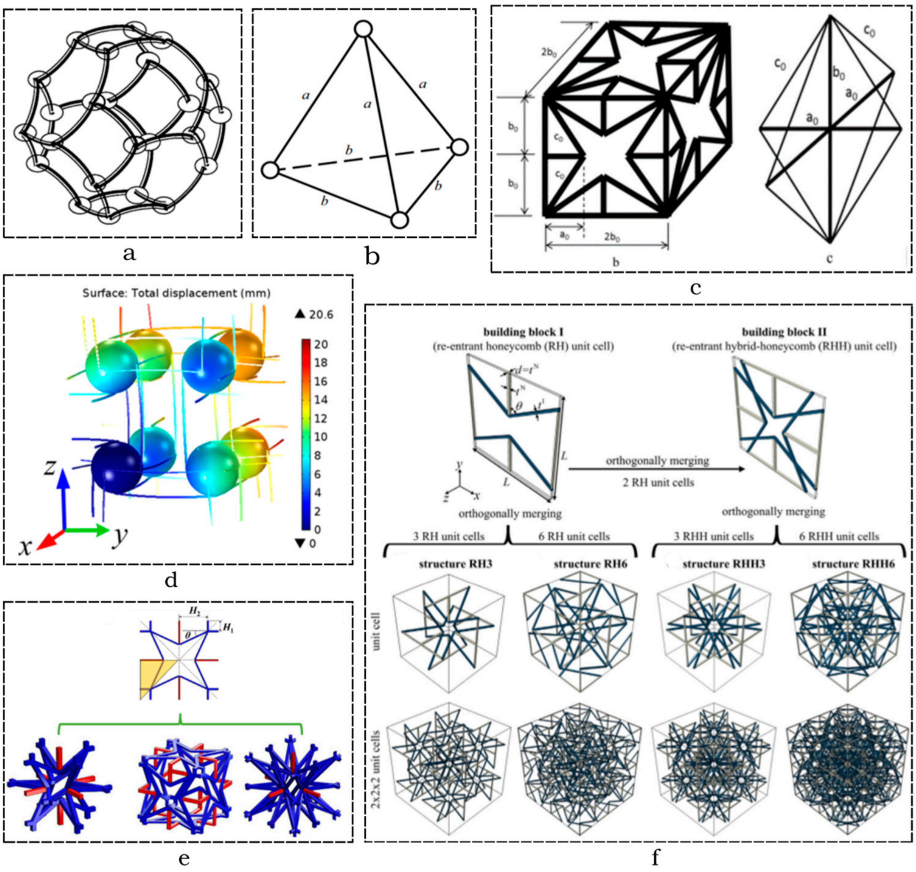

Figure 2. 3D NTE Metamaterials: (**a**) Tetrakaidecahedral foam cell with bimaterial strips (Reprinted with permission from [13]; Copyright AIP Publishing), (**b**) Negative-CTE tetrahedron with material *a* having a low CTE and material *b* having a higher CTE (Reprinted with permission from [29]; Copyright 2007 AIP Publishing), (**c**) Cubic quarter octahedral structure (Reprinted with permission from [32]; Copyright 2017 Elsevier), (**d**) Anti-chiral 3D NTE structures (Reprinted with permission from [20]; Copyright 2016 ACS Publications), (**e**) Star-shaped structures based on 2D re-entrant designs [25]; Copyright 2018 Elsevier), and (**f**) Auxetic NTE structures (Reprinted with permission from [34]; Copyright 2021 Elsevier).

Along with a difference in their design and structures, these works also vary in terms of the constituent materials used, type of analysis, fabrication methods, and achievable CTE values. Initial works in the field tend to be analytical with mathematical derivations or computational using simulation programs; however, recent works also include fabricated models of proposed architectures. A comprehensive comparison of various designs is depicted in Table 1. The fabrication methods are diverse, ranging from a basic assembly to fully 3D-printed models while the materials vary from polymers to metals.

Table 1. A comparison of NTE architectures in the literature.

Classification	Design	Researchers	Constituent Materials	CTE ($\times 10^{-6}$ m/m°C)	Type of Analysis	Fabrication Method	Ref.
				Bending-based architectures			
Bimaterial-Strip-based	Single bimaterial strip	Lakes et al.	-	Unbounded	Analytical	-	[12]
	Honeycomb lattice using bimaterial strip	Lakes et al.	Steel, invar	-10^3 to 10^3	Analytical	-	[13]
	Triangular lattice using bimaterial strip	Lehman et al.	Steel, invar	Zero, tuneable as negative or positive	Analytical	-	[14]
	Triangular and square lattices using bimaterial strip	Ha et al.	Steel, invar	Triangular lattice: −0.03 to 6.67; Square lattice: Zero	Computational	-	[36]
	Multilayered strip (three or more layers)	Grima et al.	Polyvinylidene chloride, silicone rubber	Zero to -ve values (tuneable)	Analytical, Computational	-	[19]
Chirality-based	2D triangular chiral lattice	Ha et al.	Alloy 1 (72%Mn, 18%Cu, 10%Ni), Alloy 2 (invar)	−350	Experimental	Bonding glue: Loctite type 491 cement	[16]
	2D anti-tetrachiral and trichiral lattices, 3D anti-tetrachiral lattice	Wu et al.	2D lattices: Aluminium, copper; 3D lattice: VeroWhitePlus RGD835 and TangoPlus FLX930 polymers	2D anti-tetrachiral: −70 to −35; 2D anti-trichiral: −45 to zero; 3D anti-tetrachiral: −700 to −100	Computational, Experimental	2D lattices: Screwed fittings; 3D lattice: Multimaterial polymer 3D printing (Objet350 connex2, Stratasys Ltd., Eden Prairie, MN, USA)	[20]
Re-entrant-based	Re-entrant cell-based four different 2D lattices	Ai et al.	Aluminium, steel, and invar (any two constituents per lattice)	−41 to 14.4 (Highly tuneable)	Computational	-	[26]
	Basic re-entrant unit cell lattice	Raminhos et al.	Two combinations: Nylon, Polyvinyl alcohol compound (PVA); Polypropylene (PP), Copolyester (CPE+)	−1568 to 498 in different combinations	Experimental	Fused filament fabrication 3D printing (Ultimaker 3^{TM})	[27]
	Modified re-entrant unit cell-based 2D and 3D lattices	Peng et al.	Al6061, invar	−75 to 23 for 2D; −368 to 575 for 3D; Tuneable	Analytical, Computational	-	[34,35]

Table 1. *Cont.*

Classification	Design	Researchers	Constituent Materials	CTE ($\times 10^{-6}$ m/m°C)	Type of Analysis	Fabrication Method	Ref.
Other bending-based designs	Hexagonal grid-shaped lattice	Jefferson et al.	-	Tuneable	Analytical, Computational	-	[24]
	X-shaped 2D lattice	Lim et al.	-	Tuneable	Analytical	-	[37]
				Stretch-based architectures			
Triangle-based	2D triangular lattice	Grima et al.	-	Tuneable as +ve, zero or −ve	Analytical	-	[17]
	Triangular lattice with inscribed triangles	Steeves et al.	Al7075-T6, Ti6Al4V	0 to 42	Analytical, Computational, Experimental	Laser cutting from sheets, assembly using Brazing/laser welding	[21]
	2D Hexagonal lattices	Wei et al.	Al7075, SS431, invar (Any two in one lattice)	Al–invar: −5 to Zero; Al-SS: 30; Tuneable	Analytical, Experimental	Electric discharge machining of members from sheets; Interference fit assembly using grooves	[22]
	Hoberman-sphere-inspired lattice	Li et al.	Elastomer, glassy polymer	−1040 to 10	Analytical, Computational, Experimental	Multimaterial polymer 3D printing (Objet260 Connex, Stratasys Ltd.)	[23]
Tetrahedron-based	Tetrahedral lattice	Lim et al.	-	Tuneable	Analytical	-	[29]
	Tetrahedral lattices: Stationary/non-stationary concept-based line	Xu et al.	Al6061, Ti6Al4V, invar (Al6061–Ti6Al4V and Al6061–invar combinations)	−35 to 10, Tuneable	Analytical, Computational, Experimental	Pin-jointed interference fit metallic bars bonded using epoxy glue	[31]

Table 1. *Cont.*

Classification	Design	Researchers	Constituent Materials	CTE ($\times 10^{-6}$ m/m°C)	Type of Analysis	Fabrication Method	Ref.
Octahedron-based	Cubic cell	Jin et al.	-	Tuneable +ve, zero or −ve	Analytical	-	[32]
	Octet lattice	Xu et al.	Al6061, Ti6Al4V	Aniso-octet design: −366 to 10.9; Iso-octet design: 0.273 to 11.3	Computational, Experimental	Pretension snap-fitting of laser-cut members using epoxy glue	[30]
Other designs	Ring rod sliding structure	Lim et al.	-	Tuneable as +ve, zero or −ve	Analytical	-	[28]
	Lattice-based machine frame design	Juasiripukdee et al.	Nylon 12, Ultra-high-molecular-weight polyethylene (UHMWPE)	0.001	Computational, Experimental	Nylon 12 outer part used polymer LPBF; Inner UHMWPE part used conventional manufacturing	[33]

3. Fabrication

From the previous section, it can be seen that the fabrication of negative-thermal-expansion materials requires two or more materials to be fused in a design. Multimaterial fabrication has been attempted successfully in the literature using diverse materials and various manufacturing methods, including additive and conventional manufacturing methods as well as materials like polymers and metals. This segment provides an extensive examination of diverse fabrication methods for multimaterial applications in research, their advantages and limitations, and the essential characteristics needed in multimaterial combinations to effectively generate NTE architectures.

3.1. Metal Additive Manufacturing Techniques

In the field of metal additive manufacturing (AM), PBF (powder bed fusion) and the DED (direct energy deposition) techniques stand out as the most established manufacturing processes. These methods involve adding a powdered metal or occasionally other forms like wire in DED, followed by melting using a focused thermal energy source, either simultaneously or sequentially. Unlike most additive manufacturing processes used for plastics or polymers, PBF and DED rely on electron beams, laser beams, or similar heat sources to achieve bonding between layers of metal. This is essential due to the high fusion enthalpy and melting temperatures of metals [39]. AM outperforms traditional manufacturing techniques when a high level of complexity or customization is required with a lower production volume [40]. Combined with their multimaterial fabrication capabilities, PBF and DED techniques are very promising in the fabrication of NTE metamaterials. A depiction of similarities and differences between the two processes is provided in Figure 3.

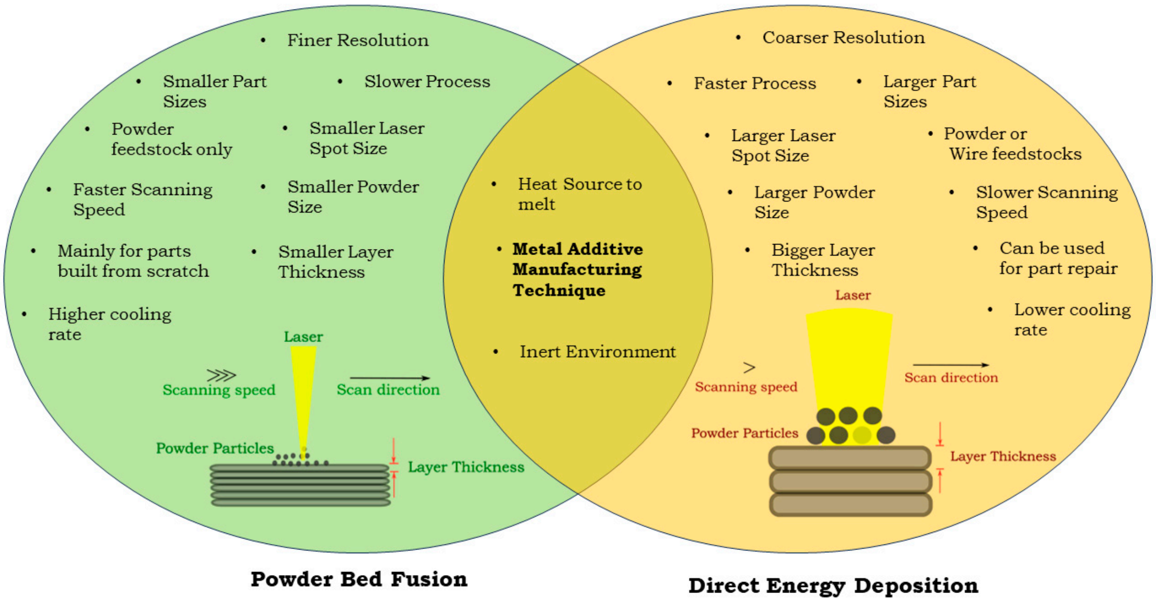

Figure 3. Comparison of powder bed fusion and direct energy deposition processes.

3.1.1. Laser Powder Bed Fusion

LPBF is an additive manufacturing technique employed to manufacture complex parts and components. A lot of metals and alloys have been successfully processed using this method. The layout of the machine usually consists of a heat source (laser or electron beam), a powder bed build platform, a powder storage system, a powder delivery system, and an overflow reservoir. Figure 4 depicts the layout of an LPBF machine. For fabrication, a substrate build plate is first fixed onto the machine's build platform and then the chamber environment is made inert primarily using nitrogen or argon.

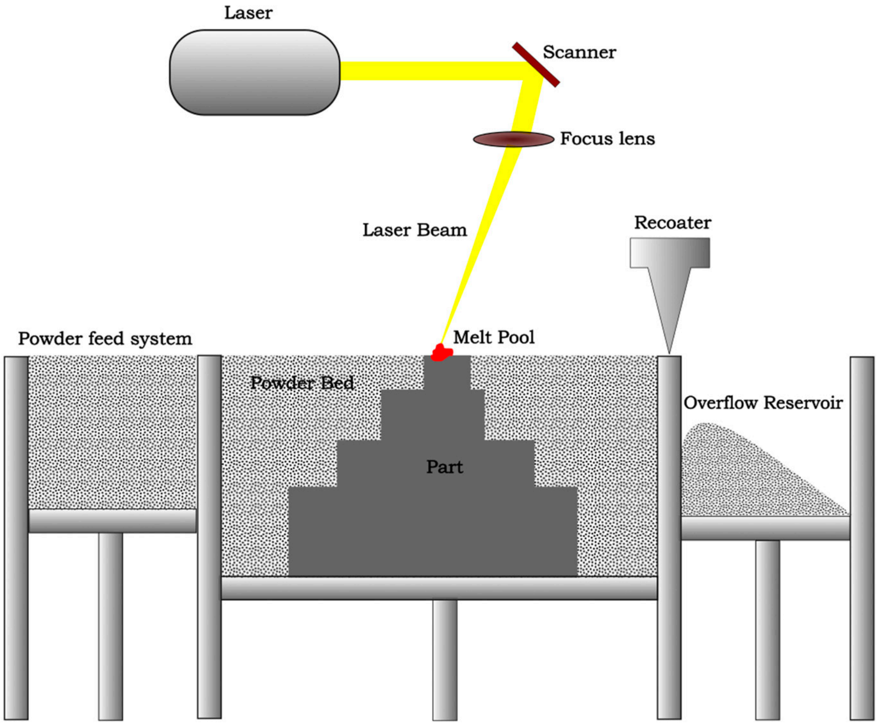

Figure 4. Laser powder bed fusion setup schematic.

After the first layer of powder is deposited based on a pre-defined layer thickness, the laser scans the powder layer in a predetermined path, thereby melting and solidifying the selected areas. Afterwards, the build platform is lowered, a new layer is deposited, and the process repeats itself until the part is fully manufactured. Initially devised for single-material parts, modifications have been made by researchers in LPBF machines to attempt to produce parts made of more than one type of material. Table 2 provides a list of the metal–metal combinations that have been successfully fabricated and industrialized. Since almost all structure-based negative expansion metamaterial designs utilize multiple materials, LPBF provides an opportunity to manufacture negative thermal expansion metamaterials. Also, as a metal-based manufacturing technique, LPBF can open doors to the production of a wide variety of NTE structures using metals in industry. The interaction of laser beams with metal powder leads to the occurrence of complex thermal and physical phenomena in the melt pool [41].

The degree of melting and rate of solidification which directly affect the produced part depend upon various factors, such as the laser power, scanning speed, hatch spacing, layer thickness, and characteristics of the metal powder used [42,43]. A list of the critical parameters in LPBF is provided in Figure 5.

However, not all materials can be successfully printed together using LPBF. The interfacial bond strength is one of the primary factors to consider when trying to attach two dissimilar metals using this technique [44–49]. A useful parameter, energy density E, is used in LPBF to calculate the effect of these multiple factors and is defined as follows [50]:

$$E = \frac{P}{v \times h \times t}$$

where P is the laser power, v is the scanning speed, h is the hatch spacing, and t is the layer thickness. If the energy density is too high, it causes splashing in the melt pool, leading to a balling effect, which can increase roughness at the surface [51]. A high E can also cause keyhole porosity formation due to metal vaporization [52,53]. A low E causes insufficient powder melting, leading to the surrounding particles sticking to contour tracks.

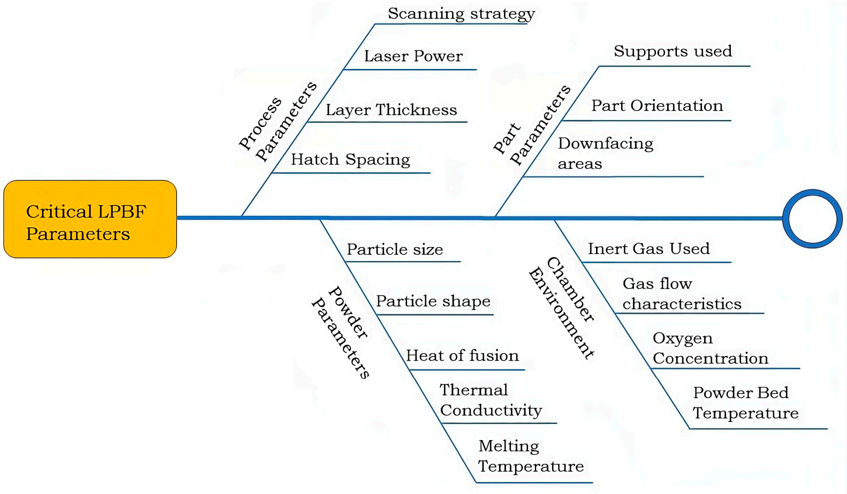

Figure 5. Critical parameters in laser powder bed fusion.

In multi-metal parts fabricated using LPBF, the optimization of energy density can reduce defects. This has been successfully observed in maraging steel–copper bimetal parts [49]. Different CTE values and thermal conductivities of steel and copper cause residual stresses, which cause weak bonding and hence induce cracking at the interface. A higher energy density tends to alleviate this problem. A decrease in residual stresses and thereby the balling effect can also be achieved by optimizing the scanning strategy. During the fabrication of SS316L and18Ni300 bimetallic structures, island and interlayer staggered scanning strategies were found to be useful [46]. In a CuSn and 18Ni300 bimetal structure, remelting scanning achieved lower levels of elongation and tensile stress [54]. The ability of LPBF to produce multimaterial prints combined with ongoing research in this direction promise the success of this process in manufacturing negative-thermal-expansion metamaterials with the limitation of smaller part sizes. Figure 6 depicts these materials in their order of fabrication.

Table 2. Various metal–metal combinations printed using LPBF.

Metal–Metal Combinations	Powders Used	References
Iron–Iron	Maraging Steel, H13 Maraging Steel, 4Cr13 Steel	[55,56]
Aluminium–Aluminium	Al12Si, Al3.5Cu1.5Mg1Si	[57]
Titanium–Titanium	Ti6Al4V, Ti5Al2.5Sn	[58]
Titanium–Iron	Ti6Al4V, K220Cu, SS316L	[59]
Titanium–Nickel	Ti6Al4V, IN718	[60]
Iron–Nickel	SS316, IN718	[45]
Copper alloy–Iron	Cu10Sn, SS316L	[44,46,61]
Pure Copper–Iron	Cu, Maraging Steel	[49]
Aluminium–Copper	AlSi10Mg, C18400	[47]
Tungsten–Copper	Pure W, CuA	[62]

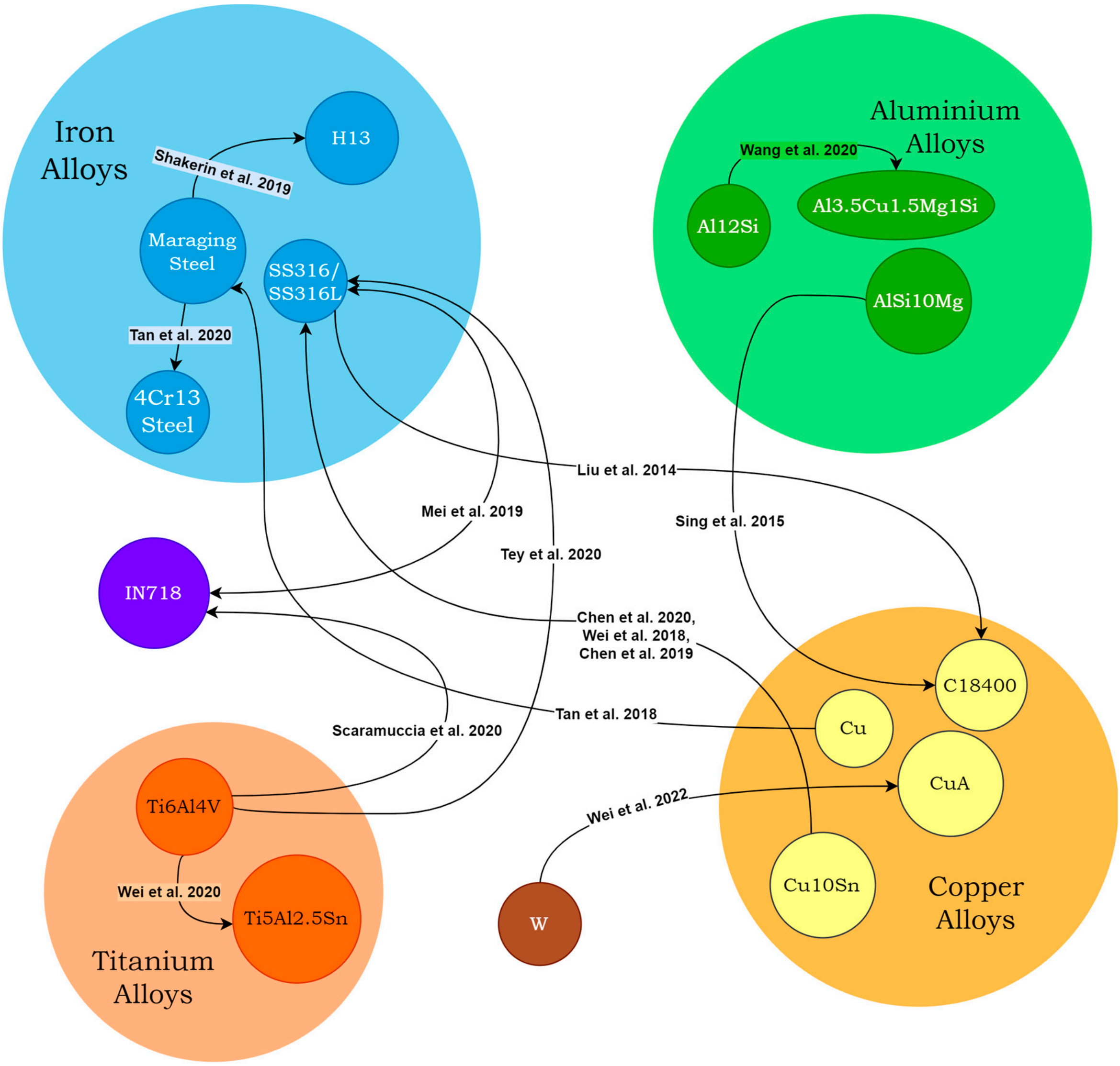

Figure 6. Multimaterial combinations fabricated using LPBF in research. The direction of arrows shows the order of fabrication of the parts (Information obtained from references [44–49,55–62]).

3.1.2. Direct Energy Deposition

DED is an additive manufacturing process that utilizes focused thermal energy to fuse materials by melting as they are being deposited (Figure 7). A heat source, like a laser or electron beam, is focused on the material being deposited, which is supplied either in the form of a blown powder or via a wire system [63,64]. Depending on the feedstock, DED processes can be classified as follows [65,66]:

9. Powder feeding;
10. Wire feeding.

A powder feeder and a laser are used in the laser additive manufacturing (LAM)–DED process [67]. Wire-based DED techniques can be classified into wire arc additive manufacturing (WAAM), wire laser additive manufacturing (WLAM), and wire electron beam additive manufacturing (WEAM), with the primary difference being the thermal energy source used to melt the wire [68–70]. WAAM uses an electric arc, WLAM uses a laser source, and WEAM uses an electron beam for melting the wire [69,70]. Various factors affect the quality of parts in DED technology. These include the type of heat source, beam size, feedstock type, feed rate, machine parameters, layer thickness, etc. (Figure 8). DED provides many key advantages, including a high material deposition rate and the ability to produce bigger parts (several meters in size) [71].

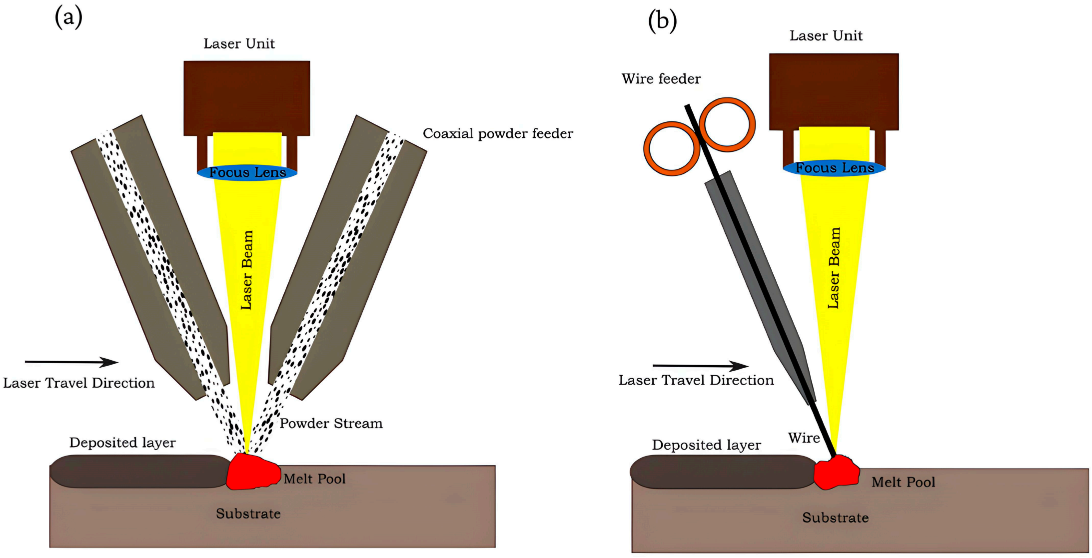

Figure 7. (**a**) Powder-based and (**b**) wire-based DED setups.

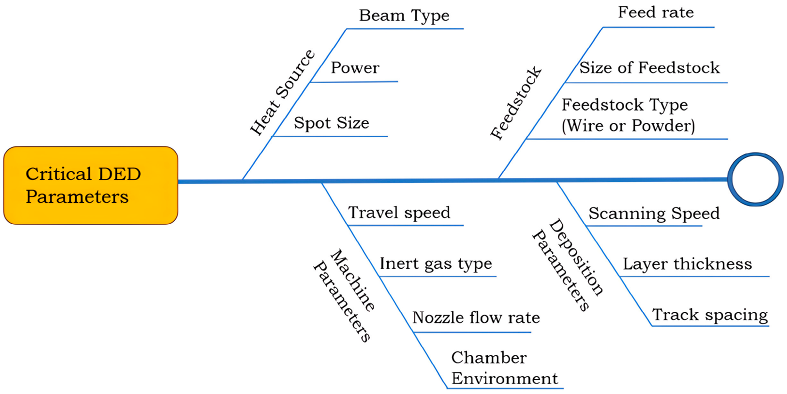

Figure 8. Critical parameters in direct energy deposition.

DED has been extensively used to produce multi-metal components in various research works [72,73]. It has been used to manufacture multimaterial structures made of Ti–alloys [74], Fe–Ni alloys [75–78], Co alloys [79], Cr alloys [80], steels [81,82] and Al–alloys [83–85]. During the fabrication of multimaterial structures, sudden transitions between material types tend to create issues. Rapid shifts in material types can pose challenges during the production of structures that use multimaterials. Issues such as the creation of fragile intermetallic phases [86], cracking during solidification [86], and elevated residual stresses due to differences in thermal expansion caused by material mismatch [87] can arise at the interfaces between materials. The problems caused by dissimilar metal bonding have been mitigated using gradient transitions between different materials, thereby forming functionally graded materials (FGMs) [88,89]. FGMs alleviate the problem of residual stresses; however, they fail to mitigate brittle intermetallic formation [76]. The technique of introducing an interfacial material at the joint of dissimilar materials has been successfully used in research to suppress intermetallic formation [90,91]. As compared to PBF, DED-manufactured parts have a coarser resolution but much bigger achievable part sizes. This leads to inefficiency in producing intricate geometries, including lattice structures which are mostly used in industry [92]. It is difficult to manufacture small-scale multimaterial lattice unit cells in this process due to the lower level of accuracy, higher surface roughness, and larger surface waviness. The process also has a lower powder recyclability and efficiency when printing a mixture of powders as compared to PBF [93]. There have been many works on multimaterial printing using DED using a wide range of alloys [94–126]. This has been represented in Figure 9.

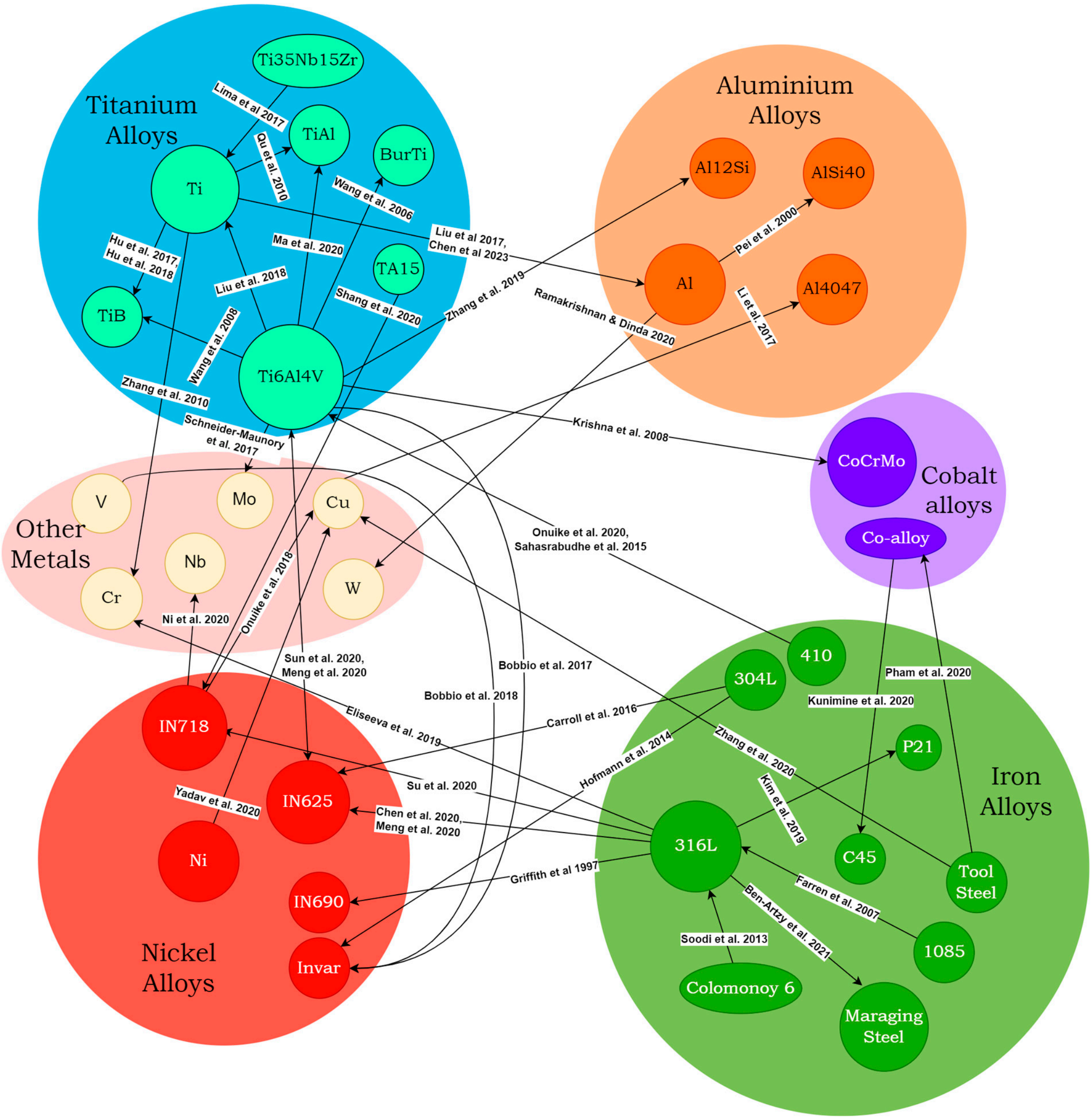

Figure 9. Multimaterial combinations fabricated using DED in research. The direction of arrows shows the order of fabrication (Information obtained from references [49,76,79,82,83,85–87,91,94–126]).

3.1.3. Polymer AM and Multimaterial Fabrication

Multimaterial manufacturing has also been tested using polymer AM techniques, like stereolithography (SLA), fused filament fabrication (FFF), direct ink writing (DIW), and PolyJet, either individually or in a combined process. SLA was the first technology in this field, using multiple vats of photopolymers to achieve its objective [127–129]. However, this approach requires a high process time [128]. Shortly afterwards, FFF, a widely used material extrusion-based technique using thermoplastic feedstock filaments, was employed for multimaterial applications by using multiple extrusion heads or nozzles [130,131]. Recently, DIW, which uses a visco-elastic ink solution using extruders, has been developed with three different apparatus modifications for multimaterial fabrication [132]. They include a single-cartridge system using a multimaterial ink with only one nozzle [133], a multicartridge system with different pastes and nozzles [134], and a concentric nozzle system with distinct filaments on core and shells [135]. A diverse array of polymers have also been considered in these studies. They include monomers; thermoplastic polymers like polyactic acid (PLA), acrylonitrile butadiene styrene (ABS), thermoplastic polyurethane (TPE), nylon, polycarbonate (PC), polycaprolactone (PCL), polyethylene terephthalate (PET) polyethylene glycol diacrylate (PEGDA), and high-impact polystyrene (HIPS); thermosetting polymers like silicones resins; and other materials like piezoelectrics, etc. (Table 3).

These processes can produce structures with multi-color regions or textures as well as spatial property variations including functional gradients. Mobilizing thermoplastic polymer chains through chemical reactions poses significant challenges, unlike thermoset plastics [136]. The prevalent use of thermoplastic polymers in hot-melt extrusion-based systems has propelled their expansion in research fields. This includes investigating the affinity between dissimilar materials and studying their mechanical properties in the production of various structures.

The critical component in polymer multimaterials is the interface established at the geometric boundary of discrete materials. This interface's characteristics depend on the properties and printing conditions of the involved materials [130]. Significant research analysing the relationship between printing parameters and the multimaterial interface is scarce in polymer AM. Thus, the field remains a potential area of investigation for future work. Other challenges include the precise alignment of various extrusion heads during multimaterial deposition as well the intermittent stoppage of plastic in one extrusion system while another material is being deposited, leading to a rheology change in the plastic and difficulties in flow rate optimization [137].

Table 3. Different material combinations in polymer AM.

Researcher	Materials Used	Reference
	Stereolithography	
Unkovskiy et al.	Silicones	[138]
Hu et al.	Monomers, PEGDA	[139]
Lu et al.	PET, Embedded piezolectrics	[140]
Jiang et al.	Different resins	[141]
	Fused Filament Fabrication	
Mansouri et al.	TPU, Bayblend	[142]
Yazdani et al.	Nylon, Carbon fibre	[143]
Lopes et al.	PLA, PET, TPU	[144]
Peng et al.	ABS, PE	
Yin et al.	ABS, TPU	[145]
Lin et al.	PLA, PCL	[146]
Mueller et al.	PET, PC	[147]
Khondoker et al.	PLA, ABS, HIPS	[148]
Ribeiro et al.	PLA, TPU	[149]
Khatri et al.	ABS, TPU	[150]
Singh et al.	ABS, HIPS	[151]
Mustafa et al.	ASA, PETG	[152]
Singh et al.	PLA, ABS, HIPS	[153]
Baca et al.	PLA, ABS, HIPS	[154]
	Direct Ink Writing	
Yirmibesoglu et al.	Elastomers	[155]
Rocha et al.	Graphene electrodes	[134]

3.2. Conventional Manufacturing Techniques and Multimaterial Fabrication

Conventional manufacturing (CM) techniques have been employed in the literature to fabricate multimaterial parts. Several CM processes, like casting, forging, and machining, as well as joining methods, like welding and riveting, have been used to produce such structures (Figure 10) [156,157]. These methods are very different than AM processes due to their shaping methodologies, utilizing both additive and subtractive approaches of manufacturing. In this section, we explore the multimaterial fabrication capabilities of these methods and juxtapose each of them with additive manufacturing (AM) processes.

3.2.1. Casting

As one of the oldest CM techniques, casting processes produce near-net-shaped parts by filling a hollow mould of the required shape with molten metal and subsequently cooling it. It is still a widely used manufacturing technique due to its affordability in producing a large number of identical parts [158]. Multimaterial part casting has been performed in the literature using the in-mould assembly technique [159]. Casting is one of the few CM techniques with the potential to produce multimaterial parts without jointing methods like rivets, adhesives, welds, or fasteners. It was first proposed by Miller to manufacture a single cast made from two different metals [160]. Gouker et al. reviewed techniques for multimaterial moulding, including cavity transfer, removable core, and sliding core techniques, and successfully used mould piece combinations to fabricate multimaterial parts [161]. Recently, there has been particular interest in producing aluminium–steel bimetallic cast parts in the literature with and without the use of coatings [162–164].

As compared to AM methods, this process is generally more affordable in producing large batch sizes of identical parts. Metal casting processes almost always require the removal of feed and filling systems from the output parts. However, parts manufactured by AM are generally closer to the final part shape with better levels of dimensional accuracy, surface finish, and customizability in terms of complexity and porosity.

3.2.2. Joining Processes

Joining processes are the primary CM methods used to join or fuse structures of different materials to fabricate multimaterial parts. Welding, a common permanent joining process, has been widely explored to fabricate multimaterial components [165]. Various welding techniques have been employed for manufacturing such components [166–168]. In particular, laser welding has several advantages, such as a high energy density and a high cooling rate with a smaller heat-affected zone [169,170]. Nevertheless, solid-state welding processes like friction and diffusion welding are better at suppressing holes and intermetallic compounds (IMCs) to generate better values of bond strength [166–168,171].

A simpler approach to joining different materials is a mechanical assembly operation. This includes processes like press fitting, shrink fitting, and even mechanical connections. Taniguchi et al. successfully used press fitting to assemble constituent parts of a bimaterial gear [172]. Shrink fitting has also been employed in research to assemble bimaterial parts [173,174].

Despite recent progress in manufacturing techniques, joining processes are still ubiquitous. AM processes are almost always more expensive than joining two components of different materials. However, in the case of multimaterial complex structures with intricate joints like lattices and gyroids, joining processes are not feasible. A similar argument exists for functionally graded multimaterial structures that have a gradual change in composition, which makes conventional joining processes redundant. Nonetheless, due to their ease of use, cost effectiveness, and versatility for simple components, these processes are widely employed in industry.

3.2.3. Forging

Forging is a manufacturing process that shapes metal using localized compressive forces to achieve the desired structure, size, and properties. These processes, broadly categorized as “hot forging”, “warm forging”, or “cold forging” have been used to produce multimaterial components [175–178]. Aluminium–steel combinations have been explored in existing studies, revealing the optimal processing conditions, with steel requiring temperatures above 900 °C and aluminium within the range of 400–500 °C. This ensures that the aluminium does not melt, and it allows for the assessment of the impact of varying values of the CTE of the two materials on their relative shrinkage [175]. Forging also has minimal feedstock waste, thereby reducing costs as compared to subtractive CM processes like machining.

In contrast to AM processes, forging has the advantage of producing larger objects more efficiently at a lower cost. The physical deformation involved in forging eliminates voids, making defects less of a concern for the mechanical performance of forged components compared to AM parts, which often exhibit some degree of porosity post-fabrication [179]. While specialized forging dies can be designed for intricate products, forging generally struggles with complex shapes. It is almost impossible to fabricate intricate designs like lattice-based structures which are generally required for metamaterials using forging. AM processes tend to perform better for relatively complex parts at a smaller production volume.

3.2.4. Machining

Machining is a subtractive manufacturing process in which a material is removed from feedstock to obtain the required shape. Currently, computer numeric control (CNC) machining is mainly used due to the high precision obtained from automation [180]. CNC machining can process a wide variety of materials, including metals, polymers, ceramics, composites, and many more. Due to the inherent subtractive nature of the process, the production of multimaterial parts generally requires the feedstock itself to be made of different materials. The multimaterial feedstock can be produced using casting, forging, or other techniques. Machining can then remove excess materials and impart the desired shape to the part.

Machining has a very prominent place in the manufacturing industry. When compared to AM, it is generally faster for not-too-complex parts at a higher volume of production. It also tends to consume comparatively less energy, although it is highly dependent on the shape and complexity of the part being manufactured. For example, the production of an aeronautical turbine using milling requires only 6 h as compared to around 16 h per part using PBF [181]. The feedstock used in machining is almost five to ten times less expensive than the metal powders used in metal AM [182]. Nonetheless, unlike metal AM, machining by itself is unable to produce multimaterial parts and requires multimaterial feedstock to be fed. Hence, it cannot be called a fully multimaterial manufacturing process. However, metal AM, as discussed before, can generate fully multimaterial products using single-material feedstocks or powders. Additionally, it is relatively easier to manufacture complex repeating-unit cell structures like lattices using metal AM, particularly PBF as compared to CNC machining [182].

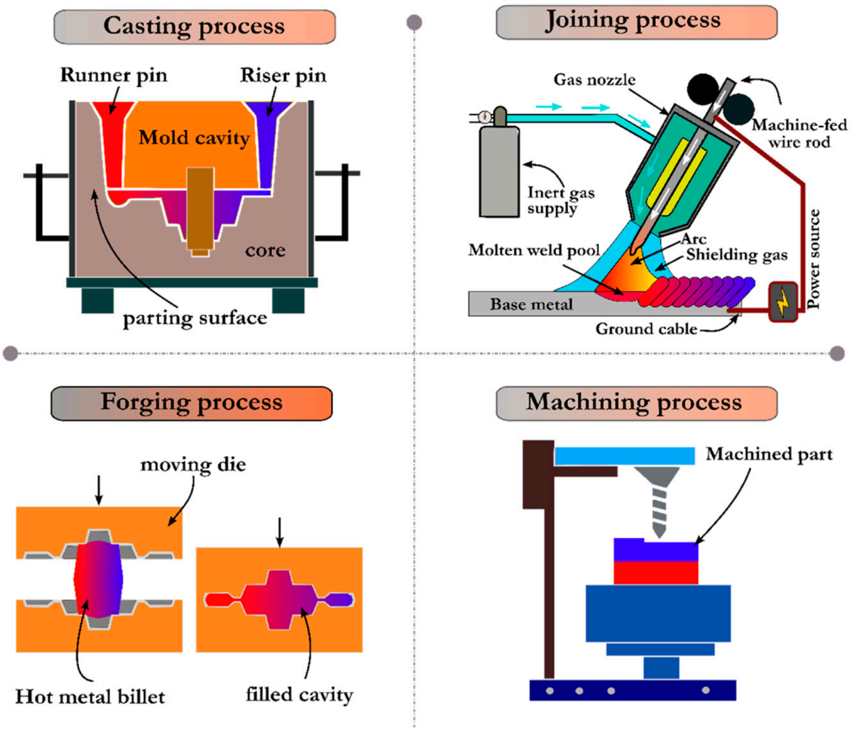

Figure 10. Schematic diagrams of various CM processes (Reprinted with permission from [179]; Copyright 2020 Hasanov et al.).

3.3. Comparison of Microstructural Properties in AM and CM Processes

In addition to the differences outlined in the preceding section, the variation in physical processes employed during production results in distinct mechanical and microstructural properties of the final parts produced through AM and CM processes. For instance, the interaction of a laser with the metallic powder in LPBF causes the formation of a tiny melt pool roughly 1 mm in length and 0.5 mm in width and depth [183,184]. Depending on various parameters, cooling rates can reach values as high as 10^3–10^8 K/s [185,186]. Based on the solidification theory for microstructure formation, grain nucleation begins at the solid–liquid interface between the base metal and melt pool [187,188]. Due to rapid solidification, homogeneous nucleation cannot take place because it usually requires a bigger time scale. Therefore, heterogeneous nucleation and epitaxial grain growth take place in LPBF with a columnar solidification front [189,190]. The final microstructure is primarily dependent on the temperature gradient at the solid–liquid interface and solidification rate. The process generally induces extremely fine microstructures in alloys like steels leading to high values of mechanical strength and hardness in the resultant parts [191,192]. Nevertheless, the selection of optimum process parameters is crucial in LPBF; otherwise, defects like holes, inclusions, and warping can easily occur and deteriorate mechanical properties [193,194]. In his work on the Inconel 625 alloy, Marchese et al. observed that DED also provides a fine microstructure; however, it is around one order of magnitude larger than LPBF [195]. It has a multi-scale non-homogeneous microstructure with columnar grains; however, the characteristic sizes exceed those in LPBF [196,197]. It leads to surface hardness and mechanical strength values that are lower than those of parts made using LPBF, but they are higher than identical parts made of wrought alloys [198]. In addition to the dependence on processing parameters, the grains observed in DED also vary with the specimen's geometry and locations within it [196,199]. Additionally, due to the differential grain flow in resultant microstructures, both LPBF and DED parts tend to show anisotropic behaviour in terms of mechanical properties [200,201].

Conventionally manufactured parts have different microstructural and mechanical properties due to differing temperature and cooling rates than AM fabricated parts. Casting can have cooling rates of 5–100 K/s, which are well below those in LPBF [202,203]. The microstructure consists of columnar elongated grains near the mould walls as opposed to equiaxed uniform grains near the core of the casting [204]. Quicker cooling promotes faster solidification, leading to finer microstructures and enhanced mechanical properties, while slower cooling leads to larger grain sizes and coarser microstructures [205,206]. However, cooling rates cannot be increased to very high values like those in AM processes because faster cooling rates can also lead to increased shrinkage and non-uniform solidification and cause voids in the final part [207]. Forging tends to elongate grains as well as defects like voids and inclusions in the direction of metal flow or plastic deformation [208]. This produces anisotropy in parts; however, the grain flow can improve properties like toughness and ductility if the crack propagation direction and grain flow directions are aligned [209]. Hot forging at high temperatures and cooling rates can also produce finer grain microstructures, thereby improving mechanical strength [210]. In fusion welding, the microstructure of the joint is predominantly determined by the filler metal's chemical composition and the amount of heat applied. A higher heat input results in a slower cooling rate, leading to larger grains, while a lower heat input speeds up cooling, producing a finer microstructure [211]. It has been observed that friction stir welding, a solid-state process, is better for hard metals like steel and titanium due to the control it provides for composition and temperature, thereby providing superior values of joint strength [212]. It directly helps to tune the microstructure and mechanical action in the form of stirring, modifying the microstructure from coarse grains to finer ones [213,214]. While in most traditional manufacturing techniques, the microstructure mainly depends on temperature history, severe plastic deformation during cutting also plays an important role in the resultant microstructure of machined parts [215]. The cutting parameters, like the depth of cut, feed rate, and cutting speed, play a huge role in microstructure development. In many works, these parameters have also been linked to phase transformation near the surface of machined parts [216–218]. The difference between AM and CM microstructures is shown in Figure 11 [219].

Clearly, these investigations establish a significant contrast in the microstructural development and mechanical characteristics of parts produced through AM and CM fabrication. The exceptionally elevated temperatures and rapid cooling associated with AM techniques tend to yield extremely fine microstructures characterized by enhanced strength, toughness, and hardness values. In contrast, different CM methods exhibit varying cooling rates, which are generally lower than those of AM processes. This results in a diverse array of possible microstructures through CM procedures, which are contingent upon the specific process and parameters employed.

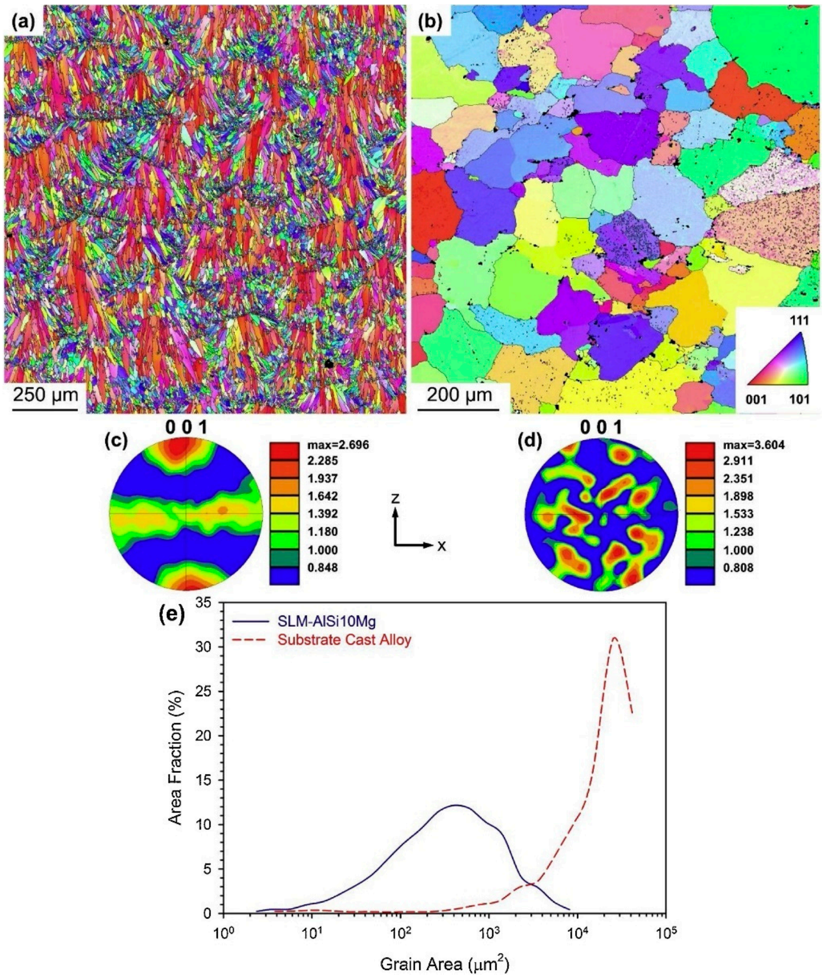

Figure 11. Electron backscatter diffraction (EBSD) maps of (**a**) LPBF-AlSi10Mg and (**b**) cast aluminium alloy. EBSD pole figures of (**c**) LPBF-AlSi10Mg and (**d**) cast aluminium alloy; (**e**) grain size area in LPBF-AlSi10Mg and the cast alloy (Reprinted with permission from [219]; Copyright 2020 Elsevier).

3.4. Material Selection for NTE Architectures

Although a multimaterial combination is necessary for NTE, this is not sufficient in itself to produce a functional NTE structure. Along with the design, an NTE metamaterial also requires the following:

11. A considerable difference in the CTE of the constituents;
12. A strong interface between different materials.

In most designs, the expansion of one material counteracts the expansion of the other to produce an overall NTE. For example, in a bimaterial strip, the material that is expanding less causes the one that is expanding more to bend, thereby leading to the shortening of the strip [12]. A high difference between the CTE values is ideal for a better NTE performance. In addition, the less-expanding material should ideally have as low a CTE value as possible for a better performance. The research conducted by Ai et al. demonstrated that all four of their NTE designs exhibited significantly lower CTE values when utilizing aluminium–invar combinations compared to steel–invar combinations, primarily due to a higher CTE difference. Conversely, the aluminium–steel combination resulted in even higher CTE values and, in some designs, an overall positive thermal expansion [26]. This outcome can be attributed to the smaller CTE difference between aluminium and steel, coupled with the fact that steel, as a material with lower expansion in the design, inherently possesses a higher CTE value than invar. Similar results were obtained by Wei et al. in their works using different combinations of Al, steel, and invar [22]. Undoubtedly, the variation in

NTE performance would be contingent on the specific design under consideration as well. Additionally, the change in CTE values for various materials with temperature could influence the performance, especially at elevated temperatures [220].

The strength of the bond at the interface is another crucial requirement in NTE metamaterials. Phase equilibrium diagrams provide essential information about stable phases under various temperatures and metallic element combinations and aid in exploring the compatibility of two metals or alloys [221]. They are helpful to evaluate the feasibility of the resultant interface strength of dissimilar alloys in different CM joining processes like welding as well as heating-based AM techniques like LPBF or DED. Not every alloy combination with a difference in CTE values and hence potential NTE fabrication capability can provide enough bond strength to the resultant interface. For instance, during the LPBF process of pure aluminium (Al) onto pure iron (Fe), an initial layer of Al powder is deposited onto the previously printed Fe. During the laser–powder interaction, not only the pure Al powder but also a portion of the solid Fe beneath it must melt to prevent cracks or a lack of fusion porosities at the Al/Fe interface. Consequently, the molten pure Al becomes diluted by Fe, and the proportion of Fe in the liquid Al depends on factors like the process parameters and powder layer thickness. Assuming 50 wt% Al and 50 wt% Fe at the interface, according to the equilibrium binary phase diagram of Fe–Al, this composition lies between the $FeAl_2$ and Fe_2Al_5 phase zones, resulting in a microstructure consisting of these two phases at room temperature (Figure 12). As the 3D printing progresses, the Fe concentration in subsequent Al layers decreases. Layers 2 to 5 might have decreasing Fe concentrations of 30, 20, 10, and 0 wt%, respectively, leading to microstructures comprising $FeAl_3$ (layer 2), (Al) + $FeAl_3$ (layers 3 and 4), and (Al). These intermetallics ($FeAl_2$, Fe_2Al_5, and $FeAl_3$) are known to be hard and brittle [222].

The LPBF process generates thermal stresses/strains that these brittle phases cannot withstand, resulting in material cracking from the interface during printing. This illustrates why Al and Fe are considered incompatible and cannot be directly printed on top of each other. The same considerations apply to printing Al-based alloys on Fe-based alloys. This phenomenon of the non-satisfactory bonding of Al–Fe from phase diagrams has already been experimentally verified in other CM joining techniques, like various welding processes and roll bonding during the joining of aluminium and iron alloys [223–226]. Therefore, it is important to identify metal or alloy combinations without intermetallics or at least avoid brittle intermetallics in their phase diagrams for compatibility in different architectures.

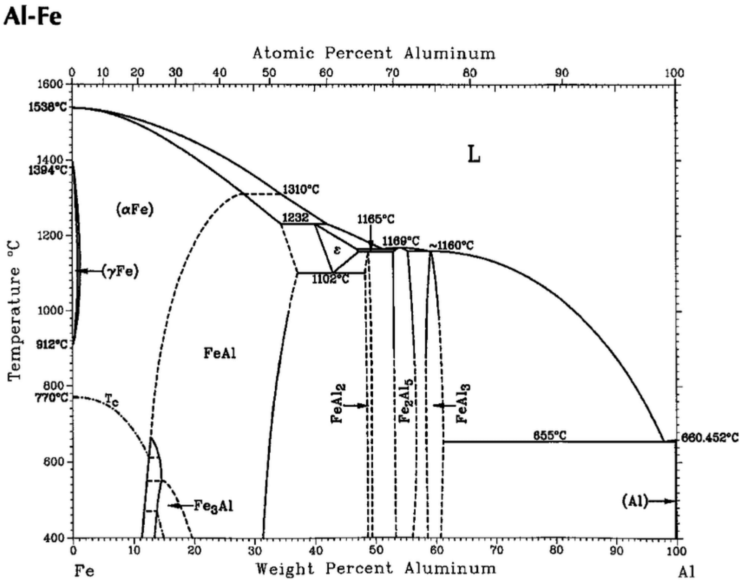

Figure 12. The iron–aluminium phase diagram (Reprinted with permission from [227]; Copyright 1990 ASM International).

On the other hand, metals like nickel (Ni) and copper (Cu) are compatible according to phase diagrams [227]. The equilibrium binary phase diagram of Ni–Cu is shown in Figure 13. As evident, no intermetallics are present in the Ni–Cu phase diagram, and these two metals can dissolve in one another at any concentration. Therefore, they are compatible and can be printed using AM processes on top of each other without any issues and even be joined using conventional joining processes like welding.

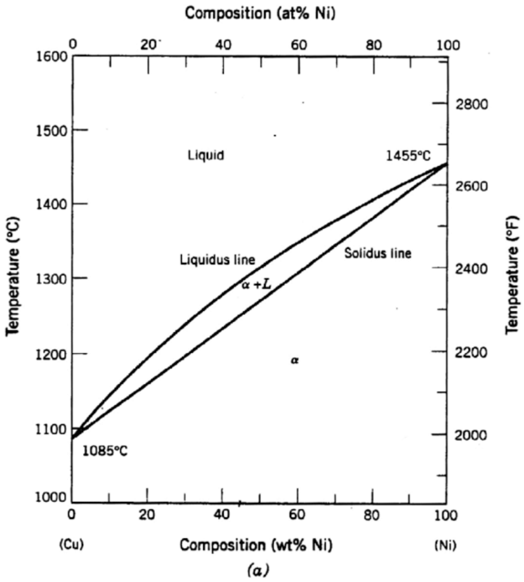

Figure 13. The copper–nickel phase diagram (Reprinted with permission from [227]; Copyright 1990 ASM International).

Nevertheless, in non-fusion joining processes like assemblies using bonding glues or riveting, this issue would not exist; however, careful attention is needed to evaluate the strength of such joints using other applicable parameters and experiments. Thus, CTE differences and material compatibility are very important requirements for the fabrication of NTE metamaterials.

4. Prospective Applications

Negative-thermal-expansion materials are in high demand for high-precision applications undergoing temperature changes. In such applications, even a minuscule dimensional change due to the expansion of their constituents can cause significant levels of inaccuracy. The combination of negative expansion structures with positive expansion materials has the potential to produce zero thermal expansion overall, leading to a high dimensional accuracy and mitigating errors in such applications. Some of these applications include the following [228–230]:

- Electronic packaging;
- Fuel cells;
- Dental implants;
- Space structures.

The sub-sections below discuss these applications in detail.

4.1. Electronic Packaging

Electronic packaging refers to the design and fabrication of enclosures for electronic devices. It is a promising application for negative- and low-expansion thermal metamaterials due to the requirement of a low CTE value for packaging constituents. For optimal thermal management, the packaging material must have the following key attributes [231]:

- High thermal conductivity (TC) to minimize thermal resistance and increase heat dissipation.
- Low CTE to minimize thermal expansion mismatches and enhance thermal cycling performance.
- High manufacturability at the micro-level.
- High mechanical strength to support and stabilize fine microstructures at high operational pressures.
- In packaging, it is vital to closely match the coefficients of thermal expansion of substrate materials to those of semiconductors, like gallium nitride and silicon carbide to avoid issues caused by CTE mismatch (Figure 14).

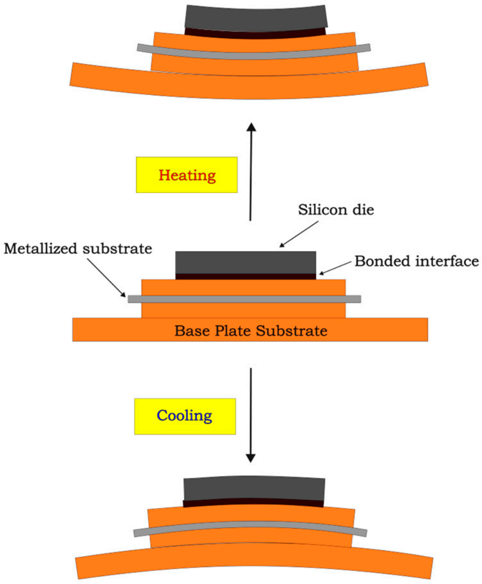

Figure 14. CTE mismatch in electronic packaging.

In order to have superior levels of heat dissipation, the substrates are also required to have high thermal conductivity values. Based on their composition, electronic packaging materials can be categorized into ceramic, plastic, and metal materials. The advantages and limitations of each are mentioned in Table 4.

Table 4. Material types used in electronic packaging.

Type of Packaging Material	Advantages	Limitations	References
Ceramic	Low CTE, low density	Low TC	[232,233]
Plastic	Small size, light weight, high impact resistance	Low TC caused by internal voids, easily corroded	[234,235]
Metal	High TC	High CTE leading to increased thermal stresses	[236,237]

A graph comparing the coefficients of the CTE values of various substrates and semiconductors is shown in Figure 15.

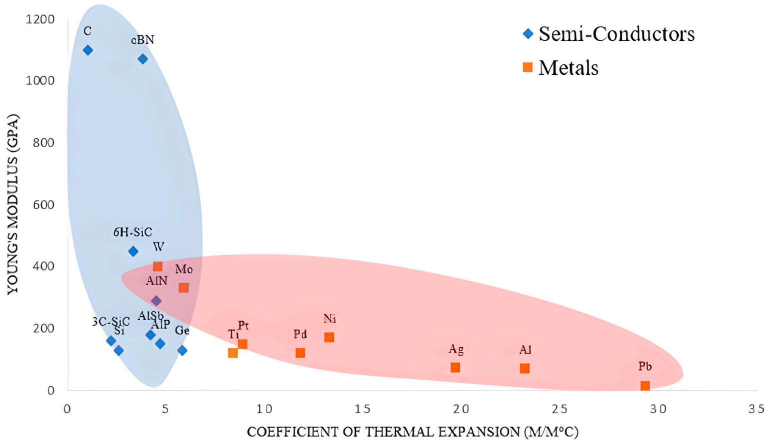

Figure 15. Young's modulus and thermal expansion coefficient of semi-conductors and metals (data obtained from [238–240]).

Unlike conventional substrates like plastics and polymers, metal substrates are particularly useful in high-temperature applications requiring higher thermal conductivity values since metals tend to have higher thermal conductivity values. Recently, thermal metamaterials have been considered for electronic packaging applications [241]. The various characteristics of thermal metamaterials' development relevant to electronic packaging applications are as follows:

- Anisotropic heat dissipation to minimize hot spots [242];
- Heat cloaking of thermally sensitive electronic components [243];
- Heat guiding in a defined path to reduce thermal interference between adjacent devices [244].

While previous research has focused mostly on inherent material properties, the architectural property of the negative thermal expansion of thermal metamaterials can be combined with the abovementioned characteristics to reduce thermal mismatch and further increase the application of metamaterials in the electronic packaging industry.

4.2. Fuel Cells

Fuel cells are electrochemical conversion devices used to generate electrical energy from chemical potential (Figure 16) [245]. Their low emission levels, silent operation, and environmentally friendly byproducts have generated interest in using them as potential replacements for fossil fuels in various applications. A summary is provided in Table 5.

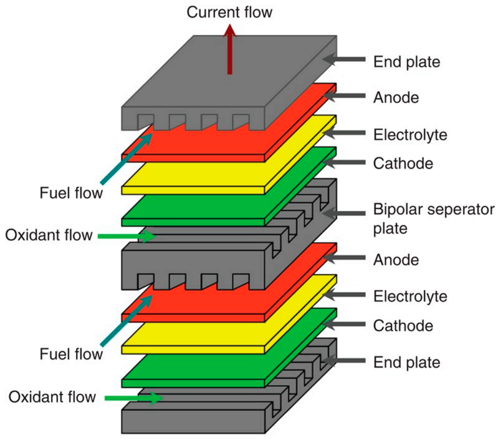

Figure 16. Design of fuel cell (Reprinted with permission from [245]; Copyright 2013 John Wiley and sons).

Table 5. Different types of fuel cells, their properties, and applications.

Type of Fuel Cell	Common Electrolyte	Operating Temperature	Efficiency	Applications	References
Proton Exchange Membrane (PEM)	Perfluoro sulfonic acid	50–100 °C	60%	Portable power, automobiles, backup power	[246]
Alkaline (AFC)	Aqueous potassium hydroxide in a matrix	90–100 °C	60%	Military, space	[247]
Phosphoric Acid (PAFC)	Phosphoric acid in a matrix	150–200 °C	40%	Distributed generation	[248]
Molten Carbonate (MCFC)	Lithium, sodium and/or potassium carbonates	600–700 °C	45–50%	Distributed generation	[249]
Solid Oxide (SOFC)	Yttria stabilized zirconia	700–1000 °C	60%	Auxiliary power, Electric utility, Distributed generation	[250,251]
Microbial Fuel Cell	Microbes	Ambient temperature	50%	Carbon capture, Wastewater treatment, Biowaste energy recovery	[252,253]

One of the emerging fuel cell types is the solid oxide fuel cell (SOFC) due to its high efficiency and diverse fuel alternatives, like carbon-based fuels. Solid oxide fuel cells (SOFCs), also known as high-temperature fuel cells, operate within the temperature range of 650 °C to 1000 °C. They use an oxygen ion conducting solid inorganic ceramic electrolyte, allowing for the utilization of a wide range of fuels. However, a significant issue with this technology is its incapacity to sustain intermittent operation. Any period of cessation and reactivation is harmful to the cell and can take several hours. One of the primary factors contributing to this problem is the varying CTE between its various components, like the electrodes, electrolyte, and interconnect materials [254–263]. A brief overview of these CTE values is shown in Table 6 [264].

Table 6. CTE values of SOFC components (Reprinted with permission from [264]; Copyright 2020 Elsevier).

Anode	CTE ($\times 10^{-6}$ K^{-1})	Electrolyte	CTE ($\times 10^{-6}$ K^{-1})	Cathode	CTE ($\times 10^{-6}$ K^{-1})	Interconnect	CTE ($\times 10^{-6}$ K^{-1})	Seals	CTE ($\times 10^{-6}$ K^{-1})
Ni-YSZ	12.2 [254]	YSZ	12.9	LSM	11.7 [255]	$LaCrO_3$	9.7 [256,257]	Ag-Cuo	15.0 [258]
LST	10.8 [259]			LSF	16.3 [260]			Soda glass	9.0 [261]
SLC	8.6–11.5			LSC LSCF LSMF SSC PSM	20.5 [260] 16.3 [260] 19.3 [262] 19.9 [263] 11.6 [260]				

Thus, thermo-mechanical instability is an important obstacle in commercial fuel cell development. The difference in the thermal expansion of various components causes high internal stresses and strains, leading to reduced durability, delamination issues, and overall higher degradation rates [265]. One of the components which suffers the most from such problems is the cathode in solid oxide fuel cells (SOFCs). Highly conductive cobalt containing perovskites, which are generally used for manufacturing due to their high oxygen reduction activity, exhibits a much higher CTE value (~20–25 × 10^{-6}/K) as compared to its SOFC electrolyte counterparts (~11.2–12.3 × 10^{-6}/K). It leads to high thermal stresses and hence frequent degradation. Techniques are utilised including doping transition metals with d^0 orbitals, making composites of perovskite material with electrolyte material, incorporating A-site deficiencies in cathodes, and introducing thermal-expansion-restricting phases [266–269]. Zhang et al. came up with the novel approach of combining an NTE material, $Y_2W_3O_{12}$ oxide (CTE~ -7×10^{-6}/K), with a Perovskite electrode material, $SrNb_{0.1}Co_{0.9}O_{3-\delta}$ (also called SNC, CTE~ 21×10^{-6}), which had a great electrochemical performance [265]. In another work, Jia et al. combined $Sm_{0.85}ZN_{0.15}MnO_3$ material exhibiting NTE with a $Ba_{0.5}Sr_{0.5}Fe_{0.8}Cu_{0.1}Ti_{0.1}O_{3-\delta}$ (BSFCT) cathode [270]. Instead of electrodes, Hayun et al. focused on altering the electrolyte's CTE by adding tungsten oxide (WO_3) powder to 8YSZ powder, which was sintered to form a tungsten-based multi-phased Yttria-stabilized zirconia (YSZ) ceramic electrolyte [264]. It has improved levels of thermal shock resistance and has the potential to reduce the problem of the lack of rapid restart in SOFCs. These multimaterial combinations show that combining different types of materials to mitigate thermal expansion issues is an emerging technique in the fuel cell industry to solve the problem of mismatch in thermal expansion. This idea is similar to the muti-material combination approach used in NTE metamaterials.

However, along with electrodes and electrolytes, the optimization of interconnects in SOFCs is also very important in fuel cells. Interconnects function as the linking components that connect the current collectors in various cells or electrical loads. The primary types of interconnects developed are (i) ceramic-based [271] and (ii) metal-based [272]. Due to the high cost and low electrical conductivity of oxide-based ceramic interconnects, recent progress has focused on metal-based interconnects. The thermal and chemical requirements of interconnect materials include the following [273]:

- Their CTE values should be similar to those of other SOFC components;
- High levels of thermal and electrical conductivity;
- High levels of mechanical strength at high temperatures;
- Chemical stability in both oxidizing and reducing environments;
- Excellent imperviousness to oxygen and hydrogen.

Metallic interconnects can be used at temperatures up to 800 °C as compared to ceramic interconnects that can be used near 1000 °C. Metallic interconnects have low material and production costs, can be easily shaped due to their high malleability, and exhibit high levels of thermal and electrical conductivity. However, they generally need protective oxide surface coatings against corrosion [274]. Ferritic stainless steels with high amounts of chromium have been extensively used due to the formation of a protective Cr_2O_3 layer at higher temperatures. Nonetheless, when exposed to elevated temperatures, chromium tends to vaporize and deposit at the cathode surface of the SOFC, thereby decreasing the life of the SOFC [272,275]. Alternative alloys with Al or Si that can create protective oxide layers like Al_2O_3 or SiO_2 are typically avoided because of their slow oxide layer development and the reason that chromium oxide (Cr_2O_3) functions as a semiconductor within the temperature range of the SOFC, therefore offering superior levels of conductivity compared to those of Al_2O_3 and SiO_2, which are electrically insulating oxides [276,277]. Nickel-based superalloys (Haynes 230, Haynes 242, Hastelloy S) offer better oxidation behaviour under the SOFC temperature range than ferritic steels like Crofer22 APU, which are commonly used SOFCs. In addition, they do not suffer from the issue of chromium evaporation, unlike ferritic steels. However, at present, nickel-based superalloys are not used in SOFCs due to their higher CTE values relative to those of other SOFC components. Additionally, in the case of Haynes 242, its CTE behaviour is non-linear [278].

NTE metamaterials, as discussed in this paper, can be used to design artificial architectures in SOFCs' interconnect design to regulate their CTE. This has the potential to make the material level CTE requirement less important and simultaneously avoid thermal stress development in SOFCs, thereby allowing researchers to use higher-CTE materials, like nickel superalloys, which offer better oxidation resistance without the chromium poisoning of the cathode.

4.3. Dental Implants

Dental implants are widely used these days to replace tooth loss caused by periodontitis, trauma, or genetic orders [279]. Their ability to integrate with bone, also called osseointegration, gives them an edge over conventional replacements like dentures or bridges [280]. Also, dental implants are standalone tooth replacements and are not attached to other teeth.

As depicted in Figure 17, the structure of a dental implant consists of the following [281]:

- Crown;
- Abutment;
- Implant body (or implant)

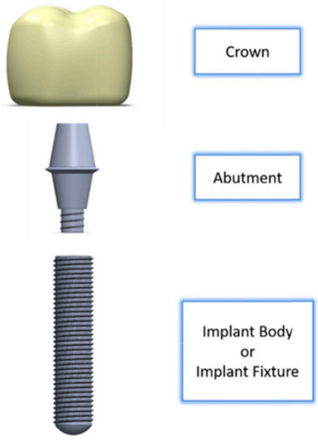

Figure 17. Structure of a general dental implant (Reprinted with permission from [281]; Copyright 2022 Elsevier).

Different types of materials have been tested for making implants. The ideal material is required to be chemically biocompatible with a fairly high mechanical strength, excellent corrosion resistance, and high wear resistance [281]. Titanium and its alloy Ti6Al4V have been widely used to manufacture these implants due to their excellent biocompatibility, lower density than that of most steels, and corrosion resistance due to the formation of oxide film TiO_2 as well as good osseointegration [282]. However, despite their advantages, these implants suffer from various issues.

- Titanium implants have a much higher Young's modulus (~120 GPa) than a typical human bone (~1 to 20 GPa). This results in the stress shielding of bone because most of the applied stress is loaded onto the implant. It can lead to lower than normal levels of stress on the surrounding bone, leading to less bone regeneration in that region and hence weaker surrounding bones over time, i.e., bone loss. This can cause the loosening of implants [283,284].
- The thermal conductivity of titanium implants is much higher than that of the human teeth they replace [285,286]. During the consumption of hot food and beverages, human teeth or dental implants undergo cyclic thermal loads. However, enamel and dentin layers in actual human teeth have low thermal conductivity, thereby protecting the sensitive inner pulp and bone inside gums from these temperature changes. However, this is not the case when dental implants are in use. These high food temperatures when transferred to alveolar bones in gums can cause permanent bone-death, also called necrosis, and the loss of bone regeneration and osseointegration. Necrosis can result from a thermal shock of 47 °C over just a minute [287,288], which can be easily caused by the excellent thermal conductivity of metal dental implants combined with intra-oral temperatures easily reaching 67–77 °C during day-to-day hot beverage consumption [289].

- Despite their biocompatibility advantages, titanium and its alloys tend to be more expensive than other implant alloy options like stainless steel [290].

NTE metamaterials have the potential to be used for dental implant applications:

- The problem of the high thermal conductivity of titanium implants can be alleviated by designing them with lattices, as used in mechanical metamaterials. Due to the porosity of lattices, the average thermal conductivity would be lower than that of a fully dense solid metal cross-section of the same size.
- The inner core of implant roots can be made of steel with a titanium covering on the outside if a negative- or low-expansion metamaterial lattice structure for a steel core is used. The low CTE of the lattice metamaterial structure would mitigate the problem of the high expansion of steels as compared to the CTE of human bone. Also, the overall cost of implants would decrease due to the lower use of titanium.

4.4. Space Structures

The fluctuating temperatures in outer space make space structures undergo thermal expansion and contraction [291]. A satellite's orbit and design, among other things, can have an impact on the severe temperature conditions that exist in space. Spacecraft materials and structures are subjected to temperatures ranging from roughly −180 °C to +180 °C during different orbital phases around Earth (Figure 18) [292]. The materials experience thermal stresses as a result of these large temperature swings, which total a 360 °C change. Differential coefficients of thermal expansion can cause issues, such as surface treatments and electronic components flaking off, as well as diminished adhesion and cracking. Other missions, such as those that investigate extra-terrestrial worlds, which may experience extended temperature ranges as well as extremely cold or high temperatures, must also consider similar concerns. Therefore, achieving almost net-zero thermal expansion is necessary for sensitive large-scale space structures, like telescopes and reflector antennas, to maintain their spatial resolution and accuracy [293,294].

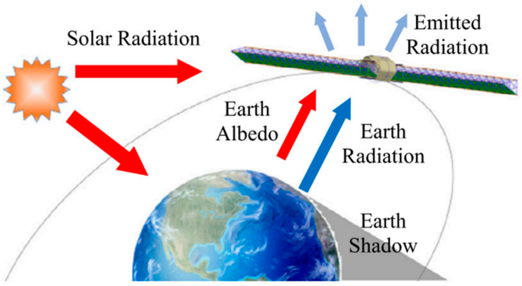

Figure 18. Fluctuating thermal environment in Earth's orbit (Reprinted with permission from [295]; Copyright 2023 Yu et al., Licensee MDPI).

Recently, thermomechanical metamaterials with tailorable low-thermal-expansion properties have garnered interest in controlling thermal expansion in space structures. Yu et al. designed two near-zero thermal expansion lattice structures using structural optimization with a negligible thermal expansion of 10^{-9} m/m.K, achieving almost zero thermal deformation. The structure also had the potential to be fabricated in orbit using additive manufacturing (Figure 19) [295]. In another work, a negative-CTE lattice structure was designed for a high-precision optical system that could be manufactured using metal additive manufacturing using invar and titanium (Figure 20) [296]. These works make a strong case for the usage of NTE metamaterials in space to mitigate thermal mismatches in various components as well as overall structure.

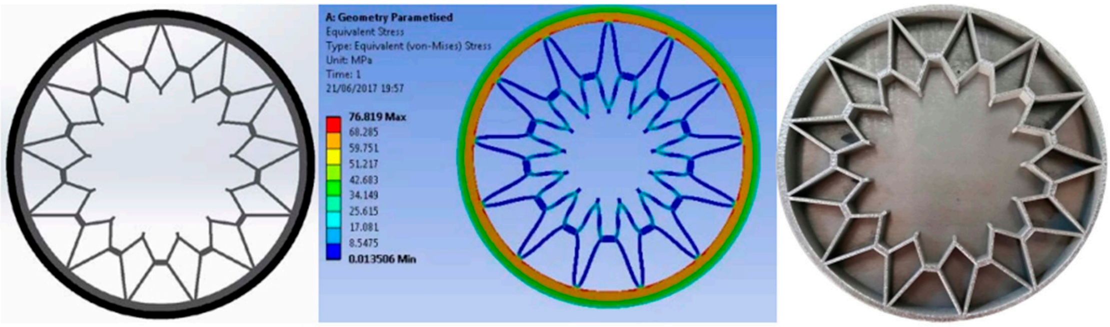

Figure 19. Negative expansion design by Milward et al. for cylindrical lens system meant for space applications (Reprinted with permission from [296]; Copyright 2017 Milward et al.).

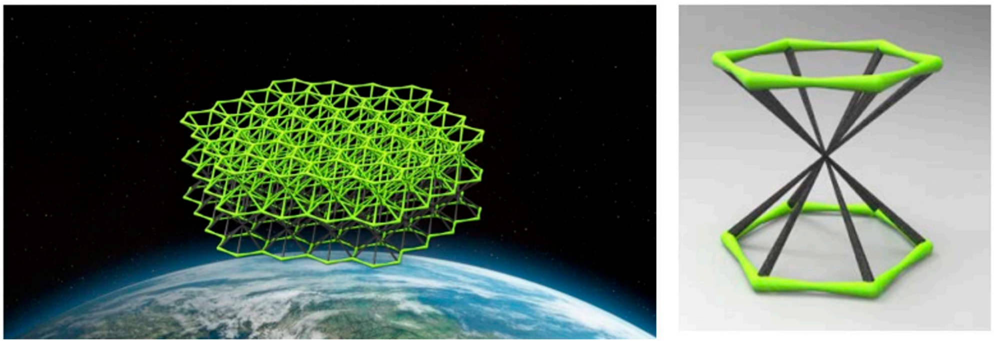

Figure 20. Bimaterial hourglass hexagonal negative expansion design by Yu et al. (Reprinted with permission from [295]; Copyright 2023 Yu et al., Licensee MDPI).

5. Conclusions

In this paper, we delved into the thriving research within the NTE metamaterials field, which has seen significant growth over the past decade. Various researchers have created numerous designs, both theoretical and experimental. Based on these findings, we can formulate the following conclusions:

- The difference between constituents directly affects the NTE performance of the design along with the CTE of lower-thermal-expansion materials. A higher difference and a lower CTE of a low-expansion material tend to decrease the overall NTE. This is a general trend with the actual performance increase varying between different architectures.
- NTE designs have been manufactured using both AM and CM processes. In contrast to traditional manufacturing techniques, AM processes can create multimetal structures in a single machine with intricate details.
- The production of these structures has been explored using both polymers and metals. Fabrication using polymers offers the advantage of creating a greater difference in CTE between constituents, as some polymers have inherently higher CTE values than metals. On the other hand, metals provided greater stiffness values to the designs because of their higher strengths.
- The properties of multimaterial structures vary depending on the processes used in their production. AM techniques, characterized by rapid cooling rates, typically yield microstructures with fine grains and high strengths. In contrast, subtractive manufacturing CM methods exhibit lower cooling rates, resulting in coarser microstructures and other distinct differences.
- Achieving strong interfacial bonds is essential when constructing practical NTE systems. In processes that involve the application of heat to join diverse materials, the bond strength relies on the miscibility of the constituents and the formation of intermediate compounds. The use of equilibrium phase diagrams plays a crucial role in understanding the resultant bond strengths in combinations of multiple materials.

- Finally, we explored the diverse applications of NTE architectures across a range of fields, including biomedicine and energy production, highlighting their versatility and the specific needs they address.

In summary, the ability to produce thermally tuned structures is a key milestone in solving the problem of mismatched thermal expansion without sacrificing mechanical strength. To achieve this, future research works are required to mainly focus on three attributes: (a) material-to-material bonding compatibility; (b) metamaterial design-to-manufacturing process compatibility; and (c) application-specific metamaterial design. Further investigations are necessary in the domain of NTE metamaterials for their successful design, production, and application. Furthermore, with the rise of AM, the utilization of metals in the creation of designs is promising, and manufacturing methods emerge as promising approaches for crafting NTE architectures with metal components. The key factor contributing to this potential is the capability of these processes to fabricate multimaterial structures with high strength values and customizable properties. PBF and DED are suitable AM techniques to produce these structures, making this a promising avenue for future research.

Author Contributions: Conceptualization, D.D.; investigation, D.D.; resources, D.D.; writing—original draft preparation, D.D.; writing—review and editing, D.D., A.S.M. and M.A.E.; supervision, M.A.E. All authors have read and agreed to the published version of the manuscript.

Funding: This research received no external funding.

Conflicts of Interest: The authors declare no conflicts of interest.

References

1. Takenaka, K. Progress of research in negative thermal expansion materials: Paradigm shift in the control of thermal expansion. *Front. Chem.* **2018**, *6*, 267. [CrossRef] [PubMed]
2. Takenaka, K. Negative thermal expansion materials: Technological key for control of thermal expansion. *Sci. Technol. Adv. Mater.* **2012**, *13*, 13001. [CrossRef] [PubMed]
3. Devoto, D.; Paret, P.; Narumanchi, S.; Mihalic, M. Reliability of Bonded Interfaces for Automotive Power Electronics. 2013. In Proceedings of the ASME 2013 International Technical Conference and Exhibition on Packaging and Integration of Electronic and Photonic Microsystems. Volume 1: Advanced Packaging; Emerging Technologies; Modeling and Simulation; Multi-Physics Based Reliability; MEMS and NEMS; Materials and Processes, Burlingame, CA, USA, 16–18 July 2013. [CrossRef]
4. Chen, J.; Hu, L.; Deng, J.; Xing, X. Negative thermal expansion in functional materials: Controllable thermal expansion by chemical modifications. *Chem. Soc. Rev.* **2015**, *44*, 3522–3567. [CrossRef] [PubMed]
5. Evans, J.S.O. Negative thermal expansion materials †. *J. Chem.Soc. DaltonTrans.* **1999**, *19*, 3317–3326. [CrossRef]
6. Chu, C.N.; Saka, N.; Suh, N.P. Negative thermal expansion ceramics: A review. *Mater. Sci. Eng.* **1987**, *95*, 303–308. [CrossRef]
7. Mary, T.A.; Evans, J.S.O.; Vogt, T.; Sleight, A.W. Negative Thermal Expansion from 0.3 to 1050 Kelvin in ZrW_2O_8. *Science* **1996**, *272*, 90–92. [CrossRef]
8. Takenaka, K.; Takagi, H. Giant negative thermal expansion in Ge-doped anti-perovskite manganese nitrides. *Appl. Phys. Lett.* **2005**, *87*, 261902. [CrossRef]
9. Greve, B.K.; Martin, K.L.; Lee, P.L.; Chupas, P.J.; Chapman, K.W.; Wilkinson, A.P. Pronounced negative thermal expansion from a simple structure: Cubic ScF_3. *J. Am. Chem. Soc.* **2010**, *132*, 15496–15498. [CrossRef]
10. Evans, J.S.O.; Mary, T.A.; Sleight, A.W. Negative Thermal Expansion in a Large Molybdate and Tungstate Family. *J. Solid State Chem.* **1997**, *133*, 580–583. [CrossRef]
11. Chapman, K.W.; Chupas, P.J.; Kepert, C.J. Compositional Dependence of Negative Thermal Expansion in the Prussian Blue Analogues MIIPtIV(CN)6 (M = Mn, Fe, Co, Ni, Cu, Zn, Cd). *J. Am. Chem. Soc.* **2006**, *128*, 7009–7014. [CrossRef]
12. Lakes, R. Cellular solid structures with unbounded thermal expansion. *J. Mater. Sci. Lett.* **1996**, *15*, 475–477. [CrossRef]
13. Lakes, R. Cellular solids with tunable positive or negative thermal expansion of unbounded magnitude. *Appl. Phys. Lett.* **2007**, *90*, 221905. [CrossRef]
14. Lehman, J.; Lakes, R. Stiff lattices with zero thermal expansion. *J. Intell. Mater. Syst. Struct.* **2012**, *23*, 1263–1268. [CrossRef]
15. Lehman, J.; Lakes, R. Stiff, strong zero thermal expansion lattices via the Poisson effect. *J. Mater. Res.* **2013**, *28*, 2499–2508. [CrossRef]
16. Ha, C.S.; Hestekin, E.; Li, J.; Plesha, M.E.; Lakes, R.S. Controllable thermal expansion of large magnitude in chiral negative Poisson's ratio lattices. *Phys. Status Solidi B Basic Res.* **2015**, *252*, 1431–1434. [CrossRef]
17. Grima, J.N.; Farrugia, P.S.; Gatt, R.; Zammit, V. A system with adjustable positive or negative thermal expansion. *Proc. R. Soc. A Math. Phys. Eng. Sci.* **2007**, *463*, 1585–1596. [CrossRef]

18. Grima, J.N.; Bajada, M.; Scerri, S.; Attard, D.; Dudek, K.K.; Gatt, R. Maximizing negative thermal expansion via rigid unit modes: A geometry-based approach. *Proc. R. Soc. A Math. Phys. Eng. Sci.* **2015**, *471*, 20150188. [CrossRef] [PubMed]
19. Grima, J.N.; Oliveri, L.; Ellul, B.; Gatt, R.; Attard, D.; Cicala, G.; Recca, G. Adjustable and negative thermal expansion from multilayered systems. *Phys. Status Solidi Rapid Res. Lett.* **2010**, *4*, 133–135. [CrossRef]
20. Wu, L.; Li, B.; Zhou, J. Isotropic Negative Thermal Expansion Metamaterials. *ACS Appl. Mater. Interfaces* **2016**, *8*, 17721–17727. [CrossRef] [PubMed]
21. Steeves, C.A.; Lucato, S.L.D.S.E.; He, M.; Antinucci, E.; Hutchinson, J.W.; Evans, A.G. Concepts for structurally robust materials that combine low thermal expansion with high stiffness. *J. Mech. Phys. Solids* **2007**, *55*, 1803–1822. [CrossRef]
22. Wei, K.; Chen, H.; Pei, Y.; Fang, D. Planar lattices with tailorable coefficient of thermal expansion and high stiffness based on dual-material triangle unit. *J. Mech. Phys. Solids* **2016**, *86*, 173–191. [CrossRef]
23. Li, Y.; Chen, Y.; Li, T.; Cao, S.; Wang, L. Hoberman-sphere-inspired lattice metamaterials with tunable negative thermal expansion. *Compos. Struct.* **2018**, *189*, 586–597. [CrossRef]
24. Jefferson, G.; Parthasarathy, T.A.; Kerans, R.J. Tailorable thermal expansion hybrid structures. *Int. J. Solids Struct.* **2009**, *46*, 2372–2387. [CrossRef]
25. Ai, L.; Gao, X.L. Three-dimensional metamaterials with a negative Poisson's ratio and a non-positive coefficient of thermal expansion. *Int. J. Mech. Sci.* **2018**, *135*, 101–113. [CrossRef]
26. Ai, L.; Gao, X.L. Metamaterials with negative Poisson's ratio and non-positive thermal expansion. *Compos. Struct.* **2017**, *162*, 70–84. [CrossRef]
27. Raminhos, J.S.; Borges, J.P.; Velhinho, A. Development of polymeric anepectic meshes: Auxetic metamaterials with negative thermal expansion. *Smart Mater. Struct.* **2019**, *28*, 45010. [CrossRef]
28. Lim, T.C. Auxetic and Negative Thermal Expansion Structure Based on Interconnected Array of Rings and Sliding Rods. *Phys. Status Solidi B Basic Res.* **2017**, *254*, 1600775. [CrossRef]
29. Lim, T.C. Negative thermal expansion structures constructed from positive thermal expansion trusses. *J. Mater. Sci.* **2012**, *47*, 368–373. [CrossRef]
30. Xu, H.; Pasini, D. Structurally efficient three-dimensional metamaterials with controllable thermal expansion. *Sci. Rep.* **2016**, *6*, 34924. [CrossRef]
31. Xu, H.; Farag, A.; Pasini, D. Routes to program thermal expansion in three-dimensional lattice metamaterials built from tetrahedral building blocks. *J. Mech. Phys. Solids* **2018**, *117*, 54–87. [CrossRef]
32. Jin, Z.H. A microlattice material with negative or zero thermal expansion. *Compos. Commun.* **2017**, *6*, 48–51. [CrossRef]
33. Juasiripukdee, P.; Maskery, I.; Ashcroft, I.; Leach, R. Low thermal expansion machine frame designs using lattice structures. *Appl. Sci.* **2021**, *11*, 9135. [CrossRef]
34. Peng, X.L.; Bargmann, S. Tunable auxeticity and isotropic negative thermal expansion in three-dimensional lattice structures of cubic symmetry. *Extreme Mech. Lett.* **2021**, *43*, 101201. [CrossRef]
35. Peng, X.L.; Bargmann, S. A novel hybrid-honeycomb structure: Enhanced stiffness, tunable auxeticity and negative thermal expansion. *Int. J. Mech. Sci.* **2021**, *190*, 106021. [CrossRef]
36. Ha, C.S.; Plesha, M.E.; Lakes, R.S. Simulations of thermoelastic triangular cell lattices with bonded joints by finite element analysis. *Extrem. Mech. Lett.* **2017**, *12*, 101–107. [CrossRef]
37. Lim, T.-C. Anisotropic and negative thermal expansion behavior in a cellular microstructure. *J. Mater. Sci.* **2005**, *40*, 3275–3277. [CrossRef]
38. Deshpande, V.S.; Ashby, M.F.; Fleck, N.A. Foam topology: Bending versus stretching dominated architectures. *Acta Mater.* **2001**, *49*, 1035–1040. [CrossRef]
39. Thompson, S.M.; Bian, L.; Shamsaei, N.; Yadollahi, A. An overview of Direct Laser Deposition for additive manufacturing; Part I: Transport phenomena, modeling and diagnostics. *Addit. Manuf.* **2015**, *8*, 36–62. [CrossRef]
40. Pereira, T.; Kennedy, J.V.; Potgieter, J. A comparison of traditional manufacturing vs additive manufacturing, the best method for the job. In *Procedia Manufacturing*; Elsevier B.V.: Amsterdam, The Netherlands, 2019; pp. 11–18. [CrossRef]
41. Ding, X.; Wang, L. Heat transfer and fluid flow of molten pool during selective laser melting of AlSi10Mg powder: Simulation and experiment. *J. Manuf. Process.* **2017**, *26*, 280–289. [CrossRef]
42. Zhang, B.; Li, Y.; Bai, Q. Defect Formation Mechanisms in Selective Laser Melting: A Review. *Chin. J. Mech. Eng. Engl. Ed.* **2017**, *30*, 515–527. [CrossRef]
43. Cao, L. Mesoscopic-scale numerical investigation including the influence of scanning strategy on selective laser melting process. *Comput. Mater. Sci.* **2021**, *189*, 110263. [CrossRef]
44. Chen, K.; Wang, C.; Hong, Q.; Wen, S.; Zhou, Y.; Yan, C.; Shi, Y. Selective laser melting 316L/CuSn10 multi-materials: Processing optimization, interfacial characterization and mechanical property. *J. Mater. Process. Technol.* **2020**, *283*, 116701. [CrossRef]
45. Mei, X.; Wang, X.; Peng, Y.; Gu, H.; Zhong, G.; Yang, S. Interfacial characterization and mechanical properties of 316L stainless steel/inconel 718 manufactured by selective laser melting. *Mater. Sci. Eng. A* **2019**, *758*, 185–191. [CrossRef]
46. Chen, J.; Yang, Y.; Song, C.; Zhang, M.; Wu, S.; Wang, D. Interfacial microstructure and mechanical properties of 316L /CuSn10 multi-material bimetallic structure fabricated by selective laser melting. *Mater. Sci. Eng. A* **2019**, *752*, 75–85. [CrossRef]
47. Sing, S.L.; Lam, L.P.; Zhang, D.Q.; Liu, Z.H.; Chua, C.K. Interfacial characterization of SLM parts in multi-material processing: Intermetallic phase formation between AlSi10Mg and C18400 copper alloy. *Mater. Charact.* **2015**, *107*, 220–227. [CrossRef]

48. Liu, Z.H.; Zhang, D.Q.; Sing, S.L.; Chua, C.K.; Loh, L.E. Interfacial characterization of SLM parts in multi-material processing: Metallurgical diffusion between 316L stainless steel and C18400 copper alloy. *Mater. Charact.* **2014**, *94*, 116–125. [CrossRef]
49. Tan, C.; Zhou, K.; Ma, W.; Min, L. Interfacial characteristic and mechanical performance of maraging steel-copper functional bimetal produced by selective laser melting based hybrid manufacture. *Mater. Des.* **2018**, *155*, 77–85. [CrossRef]
50. Thijs, L.; Verhaeghe, F.; Craeghs, T.; Van Humbeeck, J.; Kruth, J.-P. A study of the microstructural evolution during selective laser melting of Ti-6Al-4V. *Acta Mater.* **2010**, *58*, 3303–3312. [CrossRef]
51. Anwar, A.B.; Pham, Q.-C. Study of the spatter distribution on the powder bed during selective laser melting. *Addit. Manuf.* **2018**, *22*, 86–97. [CrossRef]
52. Kasperovich, G.; Haubrich, J.; Gussone, J.; Requena, G. Correlation between porosity and processing parameters in TiAl6V4 produced by selective laser melting. *Mater. Des.* **2016**, *105*, 160–170. [CrossRef]
53. King, W.E.; Barth, H.; Castillo, V.; Gallegos, G.; Gibbs, J.; Hahn, D.; Kamath, C.; Rubenchik, A. Observation of keyhole-mode laser melting in laser powder-bed fusion additive manufacturing. *J. Mater. Process. Technol.* **2014**, *214*, 2915–2925. [CrossRef]
54. Zhang, M.; Yang, Y.; Wang, D.; Song, C.; Chen, J. Microstructure and mechanical properties of CuSn/18Ni300 bimetallic porous structures manufactured by selective laser melting. *Mater. Des.* **2019**, *165*, 107583. [CrossRef]
55. Shakerin, S.; Hadadzadeh, A.; Amirkhiz, B.S.; Shamsdini, S.; Li, J.; Mohammadi, M. Additive manufacturing of maraging steel-H13 bimetals using laser powder bed fusion technique. *Addit. Manuf.* **2019**, *29*, 100797. [CrossRef]
56. Tan, C.; Zhang, X.; Dong, D.; Attard, B.; Wang, D.; Kuang, M.; Ma, W.; Zhou, K. In-situ synthesised interlayer enhances bonding strength in additively manufactured multi-material hybrid tooling. *Int. J. Mach. Tools Manuf.* **2020**, *155*, 103592. [CrossRef]
57. Wang, P.; Lao, C.; Chen, Z.; Liu, Y.; Wang, H.; Wendrock, H.; Eckert, J.; Scudino, S. Microstructure and mechanical properties of Al-12Si and Al-3.5Cu-1.5Mg-1Si bimetal fabricated by selective laser melting. *J. Mater. Sci. Technol.* **2020**, *36*, 18–26. [CrossRef]
58. Wei, K.; Zeng, X.; Li, F.; Liu, M.; Deng, J. Microstructure and Mechanical Property of Ti-5Al-2.5Sn/Ti-6Al-4V Dissimilar Titanium Alloys Integrally Fabricated by Selective Laser Melting. *JOM* **2020**, *72*, 1031–1038. [CrossRef]
59. Tey, C.F.; Tan, X.; Sing, S.L.; Yeong, W.Y. Additive manufacturing of multiple materials by selective laser melting: Ti-alloy to stainless steel via a Cu-alloy interlayer. *Addit. Manuf.* **2020**, *31*, 100970. [CrossRef]
60. Scaramuccia, M.G.; Demir, A.G.; Caprio, L.; Tassa, O.; Previtali, B. Development of processing strategies for multigraded selective laser melting of Ti6Al4V and IN718. *Powder Technol.* **2020**, *367*, 376–389. [CrossRef]
61. Wei, C.; Li, L.; Zhang, X.; Chueh, Y.H. 3D printing of multiple metallic materials via modified selective laser melting. *CIRP Ann.* **2018**, *67*, 245–248. [CrossRef]
62. Wei, C.; Liu, L.; Gu, Y.; Huang, Y.; Chen, Q.; Li, Z.; Li, L. Multi-material additive-manufacturing of tungsten–copper alloy bimetallic structure with a stainless-steel interlayer and associated bonding mechanisms. *Addit. Manuf.* **2022**, *50*, 102574. [CrossRef]
63. Frazier, W.E. Metal additive manufacturing: A review. *J. Mater. Eng. Perform.* **2014**, *23*, 1917–1928. [CrossRef]
64. Ahn, D.G. Direct metal additive manufacturing processes and their sustainable applications for green technology: A review. *Int. J. Precis. Eng. Manuf. Green Technol.* **2016**, *3*, 381–395. [CrossRef]
65. Dass, A.; Moridi, A. State of the art in directed energy deposition: From additive manufacturing to materials design. *Coatings* **2019**, *9*, 418. [CrossRef]
66. Ding, D.; Pan, Z.; Cuiuri, D.; Li, H. Wire-feed additive manufacturing of metal components: Technologies, developments and future interests. *Int. J. Adv. Manuf. Technol.* **2015**, *81*, 465–481. [CrossRef]
67. Sibisi, T.H.; Shongwe, M.B.; Tshabalala, L.C.; Mathoho, I. LAM additive manufacturing: A fundamental review on mechanical properties, common defects, dominant processing variables, and its applications. *Int. J. Adv. Manuf. Technol.* **2023**, *128*, 2847–2861. [CrossRef]
68. Williams, S.W.; Martina, F.; Addison, A.C.; Ding, J.; Pardal, G.; Colegrove, P. Wire + Arc additive manufacturing. *Mater. Sci. Technol.* **2016**, *32*, 641–647. [CrossRef]
69. Casalino, G.; Karamimoghadam, M.; Contuzzi, N. Metal Wire Additive Manufacturing: A Comparison between Arc Laser and Laser/Arc Heat Sources. *Inventions* **2023**, *8*, 52. [CrossRef]
70. Osipovich, K.; Kalashnikov, K.; Chumaevskii, A.; Gurianov, D.; Kalashnikova, T.; Vorontsov, A.; Zykova, A.; Utyaganova, V.; Panfilov, A.; Nikolaeva, A.; et al. Wire-Feed Electron Beam Additive Manufacturing: A Review. *Metals* **2023**, *13*, 279. [CrossRef]
71. Feenstra, D.R.; Banerjee, R.; Fraser, H.L.; Huang, A.; Molotnikov, A.; Birbilis, N. Critical review of the state of the art in multi-material fabrication via directed energy deposition. *Curr. Opin. Solid State Mater. Sci.* **2021**, *25*, 100924. [CrossRef]
72. Zhang, Y.; Bandyopadhyay, A. Direct fabrication of bimetallic Ti6Al4V+Al12Si structures via additive manufacturing. *Addit. Manuf.* **2019**, *29*, 100783. [CrossRef]
73. Thiriet, A.; Schneider-Maunoury, C.; Laheurte, P.; Boisselier, D.; Weiss, L. Multiscale study of different types of interface of a buffer material in powder-based directed energy deposition: Example of Ti_6Al_4V/Ti_6Al_4V—Mo/Mo—Inconel 718. *Addit. Manuf.* **2019**, *27*, 118–130. [CrossRef]
74. Zhang, J.; Zhang, Y.; Li, W.; Karnati, S.; Liou, F.; Newkirk, J.W. Microstructure and properties of functionally graded materials Ti6Al4V/TiC fabricated by direct laser deposition. *Rapid Prototyp. J.* **2018**, *24*, 677–687. [CrossRef]
75. Li, X.C.; Stampfl, J.; Prinz, F.B. Mechanical and Thermal Expansion Behavior of Laser Deposited Metal Matrix Composites of Invar and TiC. *Mater. Sci. Eng. A* **2000**, *282*, 86–90. [CrossRef]

76. Bobbio, L.D.; Bocklund, B.; Otis, R.; Borgonia, J.; Dillon, R.; Shapiro, A.; McEnerney, B.; Liu, Z.; Beese, A. Experimental analysis and thermodynamic calculations of an additively manufactured functionally graded material of v to Invar 36. *J. Mater. Res.* **2018**, *33*, 1642–1649. [CrossRef]
77. Zuback, J.S.; Palmer, T.A.; DebRoy, T. Additive manufacturing of functionally graded transition joints between ferritic and austenitic alloys. *J. Alloys Compd.* **2019**, *770*, 995–1003. [CrossRef]
78. Li, W.; Chen, X.; Yan, L.; Zhang, J.; Zhang, X.; Liou, F. Additive manufacturing of a new Fe-Cr-Ni alloy with gradually changing compositions with elemental powder mixes and thermodynamic calculation. *Int. J. Adv. Manuf. Technol.* **2018**, *95*, 1013–1023. [CrossRef]
79. Kunimine, T.; Miyazaki, R.; Yamashita, Y.; Funada, Y. Effects of Laser-Beam Defocus on Microstructural Features of Compositionally Graded WC/Co-Alloy Composites Additively Manufactured by Multi-Beam Laser Directed Energy Deposition. *Sci. Rep.* **2020**, *10*, 8975. [CrossRef] [PubMed]
80. Wang, X.; Zhang, Z.; Men, Y.; Li, X.; Liang, Y.; Ren, L. Fabrication of nano-TiC functional gradient wear-resistant composite coating on 40Cr gear steel using laser cladding under starved lubrication conditions. *Opt. Laser Technol.* **2020**, *126*, 106136. [CrossRef]
81. Lin, X.; Yue, T.M.; Yang, H.O.; Huang, W.D. Laser rapid forming of SS316L/Rene88DT graded material. *Mater. Sci. Eng. A* **2005**, *391*, 325–336. [CrossRef]
82. Ben-Artzy, A.; Reichardt, A.; Borgonia, J.; Dillon, R.; McEnerney, B.; Shapiro, A.; Hosemann, P. Compositionally graded SS316 to C300 Maraging steel using additive manufacturing. *Mater. Des.* **2021**, *201*, 109500. [CrossRef]
83. Ramakrishnan, A.; Dinda, G.P. Microstructural control of an Al–W aluminum matrix composite during direct laser metal deposition. *J. Alloys Compd.* **2020**, *813*, 152208. [CrossRef]
84. Li, J.C.; Lin, X.; Kang, N.; Lu, J.L.; Wang, Q.Z.; Huang, W.D. Microstructure, tensile and wear properties of a novel graded Al matrix composite prepared by direct energy deposition. *J. Alloys Compd.* **2020**, *826*, 154077. [CrossRef]
85. Pei, Y.T.; De Hosson, J.T.M. Functionally graded materials produced by laser cladding. *Acta Mater.* **2000**, *48*, 2617–2624. [CrossRef]
86. Chen, N.; Khan, H.; Wan, Z.; Lippert, J.; Sun, H.; Shang, S.; Liu, Z.; Li, J. Microstructural characteristics and crack formation in additively manufactured bimetal material of 316L stainless steel and Inconel 625. *Addit. Manuf.* **2020**, *32*, 101037. [CrossRef]
87. Zhang, X.; Sun, C.; Pan, T.; Flood, A.; Zhang, Y.; Li, L.; Liou, F. Additive manufacturing of copper—H13 tool steel bi-metallic structures via Ni-based multi-interlayer. *Addit. Manuf.* **2020**, *36*, 101474. [CrossRef]
88. Liu, W.; DuPont, J.N. Fabrication of functionally graded TiC/Ti composites by laser engineered net shaping. *Scr. Mater.* **2003**, *48*, 1337–1342. [CrossRef]
89. Feenstra, D.R.; Molotnikov, A.; Birbilis, N. Effect of energy density on the interface evolution of stainless steel 316L deposited upon INC 625 via directed energy deposition. *J. Mater. Sci.* **2020**, *55*, 13314–13328. [CrossRef]
90. Li, W.; Karnati, S.; Kriewall, C.; Liou, F.; Newkirk, J.; Brown Taminger, K.; Seufzer, W. Fabrication and characterization of a functionally graded material from Ti-6Al-4V to SS316 by laser metal deposition. *Addit. Manuf.* **2017**, *14*, 95–104. [CrossRef]
91. Onuike, B.; Bandyopadhyay, A. Functional bimetallic joints of Ti6Al4V to SS410. *Addit. Manuf.* **2020**, *31*, 100931. [CrossRef]
92. Babuska, T.F.; Krick, B.A.; Susan, D.F.; Kustas, A.B. Comparison of powder bed fusion and directed energy deposition for tailoring mechanical properties of traditionally brittle alloys. *Manuf. Lett.* **2021**, *28*, 30–34. [CrossRef]
93. Svetlizky, D.; Das, M.; Zheng, B.; Vyatskikh, A.; Bose, S.; Bandyopadhyay, A.; Schoenung, J.; Lavernia, E.; Eliaz, N. Directed energy deposition (DED) additive manufacturing: Physical characteristics, defects, challenges and applications. *Mater. Today* **2021**, *49*, 271–295. [CrossRef]
94. Pham, N.T.-H.; Nguyen, V.-T. Wear Properties of TiC-Reinforced Co50 Composite Coatings from Room Temperature to High Temperature. *Adv. Mater. Sci. Eng.* **2020**, *2020*, 6849081. [CrossRef]
95. Farren, J.D.; DuPont, J.N.; Noecker, F.F. Fabrication of a carbon steel-to-stainless steel transition joint using direct laser deposition-A feasibility study. *Weld. J.* **2007**, *86*, 55.
96. Kim, D.K.; Woo, W.; Kim, E.Y.; Choi, S.H. Microstructure and mechanical characteristics of multi-layered materials composed of 316L stainless steel and ferritic steel produced by direct energy deposition. *J. Alloys Compd.* **2019**, *774*, 896–907. [CrossRef]
97. Soodi, M.; Masood, S.H.; Brandt, M. Thermal expansion of functionally graded and wafer-layered structures produced by laser direct metal deposition. *Int. J. Adv. Manuf. Technol.* **2013**, *69*, 2011–2018. [CrossRef]
98. Eliseeva, O.V.; Kirk, T.; Samimi, P.; Malak, R.; Arróyave, R.; Elwany, A.; Karaman, I. Functionally Graded Materials through robotics-inspired path planning. *Mater. Des.* **2019**, *182*, 107975. [CrossRef]
99. Su, Y.; Chen, B.; Tan, C.; Song, X.; Feng, J. Influence of composition gradient variation on the microstructure and mechanical properties of 316 L/Inconel718 functionally graded material fabricated by laser additive manufacturing. *J. Mater. Process. Technol.* **2020**, *283*, 116702. [CrossRef]
100. Yadav, S.; Jinoop, A.N.; Sinha, N.; Paul, C.P.; Bindra, K.S. Parametric investigation and characterization of laser directed energy deposited copper-nickel graded layers. *Int. J. Adv. Manuf. Technol.* **2020**, *108*, 3779–3791. [CrossRef]
101. Griffith, M.L.; Harwell, L.D.; Romero, J.T.; Schlienger, E.; Atwood, C.L.; Smugeresky, J.E. Multi-Material Processing by Lens. In Proceedings of the International Solid Freeform Fabrication Symposium, Austin, TX, USA, 11–13 August 1997. [CrossRef]
102. Meng, W.; Zhang, W.; Zhang, W.; Yin, X.; Cui, B. Fabrication of steel-Inconel functionally graded materials by laser melting deposition integrating with laser synchronous preheating. *Opt. Laser Technol.* **2020**, *131*, 106451. [CrossRef]

103. Carroll, B.E.; Otis, R.; Borgonia, J.; Suh, J.; Dillon, R.; Shapiro, A.; Hofmann, D.; Liu, Z.; Beese, A. Functionally graded material of 304L stainless steel and inconel 625 fabricated by directed energy deposition: Characterization and thermodynamic modeling. *Acta Mater.* **2016**, *108*, 46–54. [CrossRef]
104. Ni, X.; Zhang, L.; Wu, W.; Zhu, D.; Kong, D.; Dong, C.; Zhu, G. Functionally Nb graded inconel 718 alloys fabricated by laser melting deposition: Mechanical properties and corrosion behavior. *Anti-Corros. Methods Mater.* **2020**, *67*, 16–23. [CrossRef]
105. Onuike, B.; Heer, B.; Bandyopadhyay, A. Additive manufacturing of Inconel 718—Copper alloy bimetallic structure using laser engineered net shaping (LENS^{TM}). *Addit. Manuf.* **2018**, *21*, 133–140. [CrossRef]
106. Chen, B.; Wang, T.; Xi, X.; Tan, C.; Song, X. Additive manufacturing of Ti-Al functionally graded material by laser based directed energy deposition. *Rapid. Prototyp. J.* **2023**, *29*, 558–568. [CrossRef]
107. Schneider-Maunoury, C.; Weiss, L.; Acquier, P.; Boisselier, D.; Laheurte, P. Functionally graded Ti6Al4V-Mo alloy manufactured with DED-CLAD® process. *Addit. Manuf.* **2017**, *17*, 55–66. [CrossRef]
108. Meng, W.; Xiaohui, Y.; Zhang, W.; Junfei, F.; Lijie, G.; Qunshuang, M.; Bing, C. Additive manufacturing of a functionally graded material from Inconel625 to Ti6Al4V by laser synchronous preheating. *J. Mater. Process. Technol.* **2020**, *275*, 116368. [CrossRef]
109. Sun, Z.; Ji, X.; Zhang, W.; Chang, L.; Xie, G.; Chang, H.; Zhou, L. Microstructure evolution and high temperature resistance of Ti_6Al_4V/Inconel625 gradient coating fabricated by laser melting deposition. *Mater. Des.* **2020**, *191*, 108644. [CrossRef]
110. Sahasrabudhe, H.; Harrison, R.; Carpenter, C.; Bandyopadhyay, A. Stainless steel to titanium bimetallic structure using LENS^{TM}. *Addit. Manuf.* **2015**, *5*, 1–8. [CrossRef]
111. Bobbio, L.D.; Otis, R.; Borgonia, J.; Dillon, R.; Shapiro, A.; Liu, Z.; Beese, A. Additive manufacturing of a functionally graded material from Ti-6Al-4V to Invar: Experimental characterization and thermodynamic calculations. *Acta Mater.* **2017**, *127*, 133–142. [CrossRef]
112. Krishna, B.V.; Xue, W.; Bose, S.; Bandyopadhyay, A. Functionally graded Co–Cr–Mo coating on Ti–6Al–4V alloy structures. *Acta Biomater.* **2008**, *4*, 697–706. [CrossRef]
113. Li, W.; Zhang, J.; Zhang, X.; Liou, F. Effect of optimizing particle size on directed energy deposition of Functionally Graded Material with blown Pre-Mixed Multi-Powder. *Manuf. Lett.* **2017**, *13*, 39–43. [CrossRef]
114. Shang, C.; Wang, C.; Li, C.; Yang, G.; Xu, G.; You, J. Eliminating the crack of laser 3D printed functionally graded material from TA15 to Inconel718 by base preheating. *Opt. Laser Technol.* **2020**, *126*, 106100. [CrossRef]
115. Wang, F.; Mei, J.; Wu, X. Direct laser fabrication of Ti6Al4V/TiB. *J. Mater. Process. Technol.* **2008**, *195*, 321–326. [CrossRef]
116. Wang, F.; Mei, J.; Wu, X. Microstructure study of direct laser fabricated Ti alloys using powder and wire. *Appl. Surf. Sci.* **2006**, *253*, 1424–1430. [CrossRef]
117. Ma, R.; Liu, Z.; Wang, W.; Xu, G.; Wang, W. Laser deposition melting of TC_4/TiAl functionally graded material. *Vacuum* **2020**, *177*, 109349. [CrossRef]
118. Qu, H.P.; Li, P.; Zhang, S.Q.; Li, A.; Wang, H.M. Microstructure and mechanical property of laser melting deposition (LMD) Ti/TiAl structural gradient material. *Mater. Des.* **2010**, *31*, 574–582. [CrossRef]
119. Liu, Y.; Liu, C.; Liu, W.; Ma, Y.; Zhang, C.; Cai, Q.; Liu, B. Microstructure and properties of Ti/Al lightweight graded material by direct laser deposition. *Mater. Sci. Technol.* **2018**, *34*, 945–951. [CrossRef]
120. Schneider-Maunoury, C.; Weiss, L.; Perroud, O.; Joguet, D.; Boisselier, D.; Laheurte, P. An application of differential injection to fabricate functionally graded Ti-Nb alloys using DED-CLAD® process. *J. Mater. Process. Technol.* **2019**, *268*, 171–180. [CrossRef]
121. Zhang, Y.Z.; Meacock, C.; Vilar, R. Laser powder micro-deposition of compositional gradient Ti–Cr alloy. *Mater. Des.* **2010**, *31*, 3891–3895. [CrossRef]
122. Liu, Y.; Liang, C.; Liu, W.; Ma, Y.; Liu, C.; Zhang, C. Dilution of Al and V through laser powder deposition enables a continuously compositionally Ti/Ti_6Al_4V graded structure. *J. Alloys Compd.* **2018**, *763*, 376–383. [CrossRef]
123. Hu, Y.; Ning, F.; Wang, H.; Cong, W.; Zhao, B. Laser engineered net shaping of quasi-continuous network microstructural TiB reinforced titanium matrix bulk composites: Microstructure and wear performance. *Opt. Laser Technol.* **2018**, *99*, 174–183. [CrossRef]
124. Hu, Y.; Zhao, B.; Ning, F.; Wang, H.; Cong, W. In-situ ultrafine three-dimensional quasi-continuous network microstructural TiB reinforced titanium matrix composites fabrication using laser engineered net shaping. *Mater. Lett.* **2017**, *195*, 116–119. [CrossRef]
125. Lima, D.D.; Mantri, S.; Mikler, C.; Contieri, R.; Yannetta, C.; Campo, K.; Lopes, E.; Styles, M.; Borkar, T.; Caram, R.; et al. Laser additive processing of a functionally graded internal fracture fixation plate. *Mater. Des.* **2017**, *130*, 8–15. [CrossRef]
126. Hofmann, D.C.; Roberts, S.; Otis, R.; Kolodziejska, J.; Dillon, R.; Suh, J.; Shapiro, A.A.; Liu, Z.; Borgonia, J. Developing Gradient Metal Alloys through Radial Deposition Additive Manufacturing. *Sci. Rep.* **2014**, *4*, 5357. [CrossRef] [PubMed]
127. Choi, J.-W.; Kim, H.-C.; Wicker, R. Multi-material stereolithography. *J. Mater. Process. Technol.* **2011**, *211*, 318–328. [CrossRef]
128. Wicker, R.; Medina, F.; Elkins, C. Muti-Material Stereolithography. US Patent US7556490B2; filed 30 July 2004 and issued 7 July 2009,
129. Inamdar, A.; Magana, M.; Medina, F.; Grajeda, Y.; Wicker, R. Development of an automated multiple material stereolithography machine. In Proceedings of the 2006 International Solid Freeform Fabrication Symposium, Austin, TX, USA, 14–16 August 2006.
130. Espalin, D.; Ramirez, J.A.; Medina, F.; Wicker, R. Multi-material, multi-technology FDM: Exploring build process variations. *Rapid Prototyp. J.* **2014**, *20*, 236–244. [CrossRef]
131. Ali, M.H.; Mir-Nasiri, N.; Ko, W.L. Multi-nozzle extrusion system for 3D printer and its control mechanism. *Int. J. Adv. Manuf. Technol.* **2016**, *86*, 999–1010. [CrossRef]

132. Rocha, V.G.; Saiz, E.; Tirichenko, I.S.; García-Tuñón, E. Direct ink writing advances in multi-material structures for a sustainable future. *J. Mater. Chem. A Mater.* **2020**, *8*, 15646–15657. [CrossRef]
133. Compton, B.G.; Lewis, J.A. 3D-Printing of Lightweight Cellular Composites. *Adv. Mater.* **2014**, *26*, 5930–5935. [CrossRef]
134. Rocha, V.G.; Garcia-Tunon, E.; Botas, C.; Markoulidis, F.; Feilden, E.; D'Elia, E.; Ni, N.; Shaffer, M.; Saiz, E. Multimaterial 3D Printing of Graphene-Based Electrodes for Electrochemical Energy Storage Using Thermoresponsive Inks. *ACS Appl. Mater. Interfaces* **2017**, *9*, 37136–37145. [CrossRef]
135. Mueller, J.; Raney, J.R.; Shea, K.; Lewis, J.A. Architected Lattices with High Stiffness and Toughness via Multicore–Shell 3D Printing. *Adv. Mater.* **2018**, *30*, 1705001. [CrossRef]
136. Nazir, A.; Gokcekaya, O.; Md Masum Billah, K.; Ertugrul, O.; Jiang, J.; Sun, J.; Hussain, S. Multi-material additive manufacturing: A systematic review of design, properties, applications, challenges, and 3D printing of materials and cellular metamaterials. *Mater. Des.* **2023**, *226*, 111661. [CrossRef]
137. Gander, J.D.; Giacomin, A.J. Review of die lip buildup in plastics extrusion. *Polym. Eng. Sci.* **1997**, *37*, 1113–1126. [CrossRef]
138. Unkovskiy, A.; Wahl, E.; Huettig, F.; Keutel, C.; Spintzyk, S. Multimaterial 3D printing of a definitive silicone auricular prosthesis: An improved technique. *J. Prosthet. Dent.* **2021**, *125*, 946–950. [CrossRef] [PubMed]
139. Hu, Q.; Rance, G.; Trindade, G.; Pervan, D.; Jiang, L.; Foerster, A.; Turyanska, L.; Tuck, C.; Irvine, D.; Hague, R.; et al. The influence of printing parameters on multi-material two-photon polymerisation based micro additive manufacturing. *Addit. Manuf.* **2022**, *51*, 102575. [CrossRef]
140. Lu, L.; Tang, X.; Hu, S.; Pan, Y. Acoustic Field-Assisted Particle Patterning for Smart Polymer Composite Fabrication in Stereolithography. *3D Print Addit. Manuf.* **2018**, *5*, 151–159. [CrossRef]
141. Jiang, C.-P.; Hentihu, M.F.R.; Lee, S.-Y.; Lin, R. Multiresin Additive Manufacturing Process for Printing a Complete Denture and an Analysis of Accuracy. *3D Print Addit. Manuf.* **2022**, *9*, 511–519. [CrossRef] [PubMed]
142. Mansouri, M.R.; Montazerian, H.; Schmauder, S.; Kadkhodapour, J. 3D-printed multimaterial composites tailored for compliancy and strain recovery. *Compos. Struct.* **2018**, *184*, 11–17. [CrossRef]
143. Sarvestani, H.Y.; Akbarzadeh, A.H.; Therriault, D.; Lévesque, M. Engineered bi-material lattices with thermo-mechanical programmability. *Compos. Struct.* **2021**, *263*, 113705. [CrossRef]
144. Lopes, L.R.; Silva, A.F.; Carneiro, O.S. Multi-material 3D printing: The relevance of materials affinity on the boundary interface performance. *Addit. Manuf.* **2018**, *23*, 45–52. [CrossRef]
145. Yin, J.; Lu, C.; Fu, J.; Huang, Y.; Zheng, Y. Interfacial bonding during multi-material fused deposition modeling (FDM) process due to inter-molecular diffusion. *Mater. Des.* **2018**, *150*, 104–112. [CrossRef]
146. Lin, W.; Shen, H.; Xu, G.; Zhang, L.; Fu, J.; Deng, X. Single-layer temperature-adjusting transition method to improve the bond strength of 3D-printed PCL/PLA parts. *Compos Part A Appl. Sci. Manuf.* **2018**, *115*, 22–30. [CrossRef]
147. Mueller, J.; Lewis, J.A.; Bertoldi, K. Architected Multimaterial Lattices with Thermally Programmable Mechanical Response. *Adv. Funct. Mater.* **2022**, *32*, 2105128. [CrossRef]
148. Khondoker, M.A.H.; Asad, A.; Sameoto, D. Printing with mechanically interlocked extrudates using a custom bi-extruder for fused deposition modelling. *Rapid Prototyp. J.* **2018**, *24*, 921–934. [CrossRef]
149. Ribeiro, M.; Carneiro, O.S.; da Silva, A.F. Interface geometries in 3D multi-material prints by fused filament fabrication. *Rapid Prototyp. J.* **2019**, *25*, 38–46. [CrossRef]
150. Khatri, N.; Egan, P. Tailored Energy Absorption for 3D Printed Multi-Material Cellular Structures Using ABS and TPU. In Proceedings of the ASME International Mechanical Engineering Congress and Exposition, Virtual, 1–5 November 2021. [CrossRef]
151. Singh, S.; Singh, N.; Gupta, M.; Prakash, C.; Singh, R. Mechanical feasibility of ABS/HIPS-based multi-material structures primed by low-cost polymer printer. *Rapid Prototyp. J.* **2019**, *25*, 152–161. [CrossRef]
152. Mustafa, I.; Kwok, T.-H. Development of Intertwined Infills to Improve Multi-Material Interfacial Bond Strength. *J. Manuf. Sci. Eng.* **2021**, *144*, 31009. [CrossRef]
153. Singh, R.; Kumar, R.; Farina, I.; Colangelo, F.; Feo, L.; Fraternali, F. Multi-material additive manufacturing of sustainable innovative materials and structures. *Polymers* **2019**, *11*, 62. [CrossRef]
154. Baca, D.; Ahmad, R. The impact on the mechanical properties of multi-material polymers fabricated with a single mixing nozzle and multi-nozzle systems via fused deposition modeling. *Int. J. Adv. Manuf. Technol.* **2020**, *106*, 4509–4520. [CrossRef]
155. Yirmibesoglu, O.D.; Simonsen, L.; Manson, R.; Davidson, J.; Healy, K.; Menguc, Y.; Wallin, T. Multi-material direct ink writing of photocurable elastomeric foams. *Commun. Mater.* **2021**, *2*, 82. [CrossRef]
156. Politis, D.J.; Politis, N.J.; Lin, J. Review of recent developments in manufacturing lightweight multi-metal gears. *Prod. Eng.* **2021**, *15*, 235–262. [CrossRef]
157. Chastel, Y.; Passemard, L. Joining Technologies for Future Automobile Multi-material Modules. *Procedia Eng.* **2014**, *81*, 2104–2110. [CrossRef]
158. Pattnaik, S.; Karunakar, D.B.; Jha, P.K. Developments in investment casting process—A review. *J. Mater. Process. Technol.* **2012**, *212*, 2332–2348. [CrossRef]
159. Priyadarshi, A.K.; Gupta, S.K.; Gouker, R.; Krebs, F.; Shroeder, M.; Warth, S. Manufacturing multi-material articulated plastic products using in-mold assembly. *Int. J. Adv. Manuf. Technol.* **2007**, *32*, 350–365. [CrossRef]
160. Miller, W.H. Gear Blanks. US Patent 3847557, filed 20 August 1973 and issued 12 November 1974.

161. Gouker, R.M.; Gupta, S.K.; Bruck, H.A.; Holzschuh, T. Manufacturing of multi-material compliant mechanisms using multi-material molding. *Int. J. Adv. Manuf. Technol.* **2006**, *30*, 1049–1075. [CrossRef]
162. Bakke, A.O.; Nordmark, A.; Arnberg, L.; Li, Y. Sn-Aided Joining of Cast Aluminum and Steel Through a Compound Casting Process. *Metall. Mater. Trans. B* **2022**, *53*, 60–70. [CrossRef]
163. Locke, C.; Guggemos, M.; Gruber, M.; Maier, L.; Mayr, L.; Weiß, T.; Volk, W.; Günther, D. Compound Casting of Aluminum with Sheet Steel in 3D Sand Casting Using an Inductive Heating System. *Metals* **2023**, *13*, 354. [CrossRef]
164. Moodispaw, M.P.; Chen, B.; Luo, A.A.; Wang, Q. Achieving Metallurgical Bonding in Aluminum/Steel Bimetallic Castings. *Int. J. Met.* **2024**. [CrossRef]
165. Fang, Y.; Jiang, X.; Mo, D.; Zhu, D.; Luo, Z. A review on dissimilar metals' welding methods and mechanisms with interlayer. *Int. J. Adv. Manuf. Technol.* **2019**, *102*, 2845–2863. [CrossRef]
166. Kuang, B.; Shen, Y.; Chen, W.; Yao, X.; Xu, H.; Gao, J.; Zhang, J. The dissimilar friction stir lap welding of 1A99 Al to pure Cu using Zn as filler metal with 'pinless' tool configuration. *Mater. Des.* **2015**, *68*, 54–62. [CrossRef]
167. Liu, L.; Ren, D.; Liu, F. A review of dissimilar welding techniques for magnesium alloys to aluminum alloys. *Materials* **2014**, *7*, 3735–3757. [CrossRef]
168. Yu, W.; Zhao, H.; Huang, Z.; Chen, X.; Aman, Y.; Li, S.; Zhai, H.; Guo, Z.; Xiong, S. Microstructure evolution and bonding mechanism of Ti2SnC-Ti6Al4V joint by using Cu pure foil interlayer. *Mater. Charact.* **2017**, *127*, 53–59. [CrossRef]
169. Peyre, P.; Berthe, L.; Dal, M.; Pouzet, S.; Sallamand, P.; Tomashchuk, I. Generation and characterization of T40/A5754 interfaces with lasers. *J. Mater. Process. Technol.* **2014**, *214*, 1946–1953. [CrossRef]
170. Li, L.; Tan, C.; Chen, Y.; Guo, W.; Song, F. Comparative study on microstructure and mechanical properties of laser welded–brazed Mg/mild steel and Mg/stainless steel joints. *Mater. Des.* **2013**, *43*, 59–65. [CrossRef]
171. Hossain, M.A.M.; Hasan, M.T.; Hong, S.-T.; Miles, M.; Cho, H.-H.; Han, H.N. Mechanical Behaviors of Friction Stir Spot Welded Joints of Dissimilar Ferrous Alloys under Opening-Dominant Combined Loads. *Adv. Mater. Sci. Eng.* **2014**, *2014*, 572970. [CrossRef]
172. Taniguchi, M.; Ukai, Y.; Tsunekawa, H.; Shioiri, H. Structure for Fastening Ring Gear to Differential Case, and Differential Device Employing Same. U.S. Patent US2013/0074649 A1, filed 4 June 2010 and issued 28 March 2013.
173. Matsumoto, R.; Hanami, S.; Ogura, A.; Yoshimura, H.; Osakada, K. New plastic joining method using indentation of cold bar to hot forged part. *CIRP Ann.* **2008**, *57*, 279–282. [CrossRef]
174. Qiao, J.; Kou, S.Q.; He, D.Y.; Yang, S.H. Torque Strength and Influencing Factors Analysis for Assembled Camshaft by Knurling Joining. *Mater. Sci. For.* **2008**, *575–578*, 216–221. [CrossRef]
175. Wohletz, S.; Groche, P. Temperature Influence on Bond Formation in Multi-material Joining by Forging. *Procedia Eng.* **2014**, *81*, 2000–2005. [CrossRef]
176. Meng, Z.; Jia, X.; Feng, W.; Zhuang, W.; Wu, M. Investigation on Interfacial Bonding Characteristics of Steel/Aluminum Bi-Metal Gears by Hot Forging Processing. *Metals* **2022**, *12*, 1244. [CrossRef]
177. Behrens, B.-A.; Kosch, K.-G. Development of the heating and forming strategy in compound forging of hybrid steel-aluminum parts. *Mater. Werkst.* **2011**, *42*, 973–978. [CrossRef]
178. Kriwall, M.; Stonis, M.; Bick, T.; Treutler, K.; Wesling, V. Dependence of the Joint Strength on Different Forming Steps and Geometry in Hybrid Compound Forging of Bulk Aluminum Parts and Steel Sheets. *Procedia Manuf.* **2020**, *47*, 356–361. [CrossRef]
179. Hasanov, S.; Alkunte, S.; Rajeshirke, M.; Gupta, A.; Huseynov, O.; Fidan, I.; Alifui-Segbaya, F.; Rennie, A. Review on additive manufacturing of multi-material parts: Progress and challenges. *J. Manuf. Mater. Process.* **2022**, *6*, 4. [CrossRef]
180. Okokpujie, I.P.; Bolu, C.A.; Ohunakin, O.S.; Akinlabi, E.T.; Adelekan, D.S. A Review of Recent Application of Machining Techniques, based on the Phenomena of CNC Machining Operations. *Procedia Manuf.* **2019**, *35*, 1054–1060. [CrossRef]
181. Paris, H.; Mokhtarian, H.; Coatanéa, E.; Museau, M.; Ituarte, I.F. Comparative environmental impacts of additive and subtractive manufacturing technologies. *CIRP Ann.* **2016**, *65*, 29–32. [CrossRef]
182. Laureijs, R.E.; Roca, J.B.; Narra, S.P.; Montgomery, C.; Beuth, J.L.; Fuchs, E.R.H. Metal Additive Manufacturing: Cost Competitive Beyond Low Volumes. *J. Manuf. Sci. Eng.* **2017**, *139*, 81010. [CrossRef]
183. Ilin, A.; Logvinov, R.; Kulikov, A.; Prihodovsky, A.; Xu, H.; Ploshikhin, V.; Günther, B.; Bechmann, F. Computer Aided Optimisation of the Thermal Management During Laser Beam Melting Process. *Phys. Procedia* **2014**, *56*, 390–399. [CrossRef]
184. Hussein, A.; Hao, L.; Yan, C.; Everson, R. Finite element simulation of the temperature and stress fields in single layers built without-support in selective laser melting. *Mater. Des.* **2013**, *52*, 638–647. [CrossRef]
185. Gu, D.D.; Meiners, W.; Wissenbach, K.; Poprawe, R. Laser additive manufacturing of metallic components: Materials, processes and mechanisms. *Int. Mater. Rev.* **2012**, *57*, 133–164. [CrossRef]
186. Jung, H.Y.; Choi, S.; Prashanth, K.; Stoica, M.; Scudino, S.; Yi, S.; Kühn, U.; Kim, D.; Kim, K.; Eckert, J. Fabrication of Fe-based bulk metallic glass by selective laser melting: A parameter study. *Mater. Des.* **2015**, *86*, 703–708. [CrossRef]
187. Gäumann, M.; Henry, S.; Cléton, F.; Wagnière, J.-D.; Kurz, W. Epitaxial laser metal forming: Analysis of microstructure formation. *Mater. Sci. Eng. A* **1999**, *271*, 232–241. [CrossRef]
188. Wang, C.; Zhang, J.; Liu, L.; Fu, H. Effect of Melt Superheating Treatment on Directional Solidification Interface Morphology of Multi-component Alloy. *J. Mater. Sci. Technol.* **2011**, *27*, 668–672. [CrossRef]
189. Shi, Q.; Gu, D.; Xia, M.; Cao, S.; Rong, T. Effects of laser processing parameters on thermal behavior and melting/solidification mechanism during selective laser melting of TiC/Inconel 718 composites. *Opt. Laser Technol.* **2016**, *84*, 9–22. [CrossRef]

190. Garibaldi, M.; Ashcroft, I.; Simonelli, M.; Hague, R. Metallurgy of high-silicon steel parts produced using Selective Laser Melting. *Acta Mater.* **2016**, *110*, 207–216. [CrossRef]
191. Deng, Q.L.; Xie, A.N.; Ge, Z.J.; Song, J.L. Experimental Researches on Rapid Forming Full Compacted Metal Parts by Selective Laser Melting. *Mater. Sci. For.* **2006**, *532–533*, 428–431. [CrossRef]
192. Cherry, J.A.; Davies, H.M.; Mehmood, S.; Lavery, N.P.; Brown, S.G.R.; Sienz, J. Investigation into the effect of process parameters on microstructural and physical properties of 316L stainless steel parts by selective laser melting. *Int. J. Adv. Manuf. Technol.* **2015**, *76*, 869–879. [CrossRef]
193. Narasimharaju, S.R.; Liu, W.; Zeng, W.; See, T.; Scott, P.; Jiang, X.; Lou, S. Surface Texture Characterization of Metal Selective Laser Melted Part with Varying Surface Inclinations. *J. Tribol.* **2021**, *143*, 51106. [CrossRef]
194. Kadkhodapour, J.; Mirhakimi, A.S.; Montazerian, H. Chapter Four—Structural defects and mechanical properties of additively manufactured parts. In *Quality Analysis of Additively Manufactured Metals*; Kadkhodapour, J., Schmauder, S., Sajadi, F., Eds.; Elsevier: Amsterdam, The Netherlands, 2023; pp. 119–172. [CrossRef]
195. Marchese, G.; Garmendia Colera, X.; Calignano, F.; Lorusso, M.; Biamino, S.; Minetola, P.; Manfredi, D. Characterization and Comparison of Inconel 625 Processed by Selective Laser Melting and Laser Metal Deposition. *Adv. Eng. Mater.* **2017**, *19*, 1600635. [CrossRef]
196. Dinda, G.P.; Dasgupta, A.K.; Mazumder, J. Laser aided direct metal deposition of Inconel 625 superalloy: Microstructural evolution and thermal stability. *Mater. Sci. Eng. A* **2009**, *509*, 98–104. [CrossRef]
197. Sateesh, N.H.; Kumar, G.C.M.; Prasad, K.; Srinivasa, C.K.; Vinod, A.R. Microstructure and Mechanical Characterization of Laser Sintered Inconel-625 Superalloy. *Procedia Mater. Sci.* **2014**, *5*, 772–779. [CrossRef]
198. Martin, N.; Hor, A.; Copin, E.; Lours, P.; Ratsifandrihana, L. Correlation between microstructure heterogeneity and multi-scale mechanical behavior of hybrid LPBF-DED Inconel 625. *J. Mater. Process. Technol.* **2022**, *303*, 117542. [CrossRef]
199. Ma, D.; Stoica, A.D.; Wang, Z.; Beese, A.M. Crystallographic texture in an additively manufactured nickel-base superalloy. *Mater. Sci. Eng. A* **2017**, *684*, 47–53. [CrossRef]
200. Dixit, S.; Liu, S.; Murdoch, H.A.; Smith, P.M. Investigating build orientation-induced mechanical anisotropy in additive manufacturing 316L stainless steel. *Mater. Sci. Eng. A* **2023**, *880*, 145308. [CrossRef]
201. Wolff, S.; Lee, T.; Faierson, E.; Ehmann, K.; Cao, J. Anisotropic properties of directed energy deposition (DED)-processed Ti–6Al–4V. *J. Manuf. Process.* **2016**, *24*, 397–405. [CrossRef]
202. Žbontar, M.; Petrič, M.; Mrvar, P. The influence of cooling rate on microstructure and mechanical properties of alsi9cu3. *Metals* **2021**, *11*, 186. [CrossRef]
203. Górny, M.; Tyrała, E. Effect of Cooling Rate on Microstructure and Mechanical Properties of Thin-Walled Ductile Iron Castings. *J. Mater. Eng. Perform.* **2013**, *22*, 300–305. [CrossRef]
204. Mouritz, A.P. (Ed.) 6—Production and casting of aerospace metals. In *Introduction to Aerospace Materials*; Woodhead Publishing: Sawston, UK, 2012; pp. 128–153. [CrossRef]
205. Pang, S.; Wu, G.; Liu, W.; Sun, M.; Zhang, Y.; Liu, Z.; Ding, W. Effect of cooling rate on the microstructure and mechanical properties of sand-casting Mg–10Gd–3Y–0.5Zr magnesium alloy. *Mater. Sci. Eng. A* **2013**, *562*, 152–160. [CrossRef]
206. Gong, L.; Chen, B.; Zhang, L.; Ma, Y.; Liu, K. Effect of cooling rate on microstructure, microsegregation and mechanical properties of cast Ni-based superalloy K417G. *J. Mater. Sci. Technol.* **2018**, *34*, 811–820. [CrossRef]
207. Papanikolaou, M.; Saxena, P. Chapter 7—Sustainable casting processes through simulation-driven optimization. In *Sustainable Manufacturing*; Gupta, K., Salonitis, K., Eds.; Elsevier: Amsterdam, The Netherlands, 2021; pp. 165–198. [CrossRef]
208. Yamabe-Mitarai, Y.; Kuroda, S.; Motohashi, N.; Matsumoto, H.; Miyamoto, G.; Chandiran, E.; Yoshida, Y.; Itsumi, Y. Effect of Forging Temperature on Microstructure Evolution and Tensile Properties of Ti-17 Alloys. *Mater. Trans* **2019**, *60*, 1733–1739. [CrossRef]
209. Suris, J.A.; Yurgel, C.C.; de Sousa, R.A. Influence of the Grain-Flow Orientation after Hot Forging Process Evaluated through Rotational Flexing Fatigue Test. *Metals* **2023**, *13*, 187. [CrossRef]
210. Zhou, J.; Liao, H.; Chen, H.; Huang, A. Effects of hot-forging and subsequent annealing on microstructure and mechanical behaviors of Fe35Ni35Cr20Mn10 high-entropy alloy. *Mater. Charact.* **2021**, *178*, 111251. [CrossRef]
211. ZHANG, Y.; ZHANG, H.; LI, J.; LIU, W. Effect of Heat Input on Microstructure and Toughness of Coarse Grain Heat Affected Zone in Nb Microalloyed HSLA Steels. *J. Iron Steel Res. Int.* **2009**, *16*, 73–80. [CrossRef]
212. Fujii, H.; Cui, L.; Tsuji, N.; Maeda, M.; Nakata, K.; Nogi, K. Friction stir welding of carbon steels. *Mater. Sci. Eng. A* **2006**, *429*, 50–57. [CrossRef]
213. Zhu, X.K.; Chao, Y.J. Numerical simulation of transient temperature and residual stresses in friction stir welding of 304L stainless steel. *J. Mater. Process. Technol.* **2004**, *146*, 263–272. [CrossRef]
214. Park, S.H.C.; Sato, Y.S.; Kokawa, H.; Okamoto, K.; Hirano, S.; Inagaki, M. Boride Formation Induced by pcBN Tool Wear in Friction-Stir-Welded Stainless Steels. *Metall. Mater. Trans. A* **2009**, *40*, 625–636. [CrossRef]
215. Pan, Z.; Feng, Y.; Liang, S.Y. Material microstructure affected machining: A review. *Manuf. Rev.* **2017**, *4*, 5. [CrossRef]
216. Meyers, M.A.; Xu, Y.B.; Xue, Q.; Pérez-Prado, M.T.; McNelley, T.R. Microstructural evolution in adiabatic shear localization in stainless steel. *Acta Mater.* **2003**, *51*, 1307–1325. [CrossRef]
217. Chuzhoy, L.; DeVor, R.E.; Kapoor, S.G.; Bammann, D.J. Microstructure-Level Modeling of Ductile Iron Machining. *J. Manuf. Sci. Eng.* **2002**, *124*, 162–169. [CrossRef]

218. Xu, Y.; Zhang, J.; Bai, Y.; Meyers, M.A. Shear Localization in Dynamic Deformation: Microstructural Evolution. *Metall. Mater. Trans. A* **2008**, *39*, 811–843. [CrossRef]
219. Hadadzadeh, A.; Amirkhiz, B.S.; Shakerin, S.; Kelly, J.; Li, J.; Mohammadi, M. Microstructural investigation and mechanical behavior of a two-material component fabricated through selective laser melting of $AlSi_{10}Mg$ on an Al-Cu-Ni-Fe-Mg cast alloy substrate. *Addit. Manuf.* **2020**, *31*, 100937. [CrossRef]
220. Kanagaraj, S.; Pattanayak, S. Measurement of the thermal expansion of metal and FRPs. *Cryogenics* **2003**, *43*, 399–424. [CrossRef]
221. Wang, F.E. Chapter 2—Phase Equilibrium Diagrams. In *Bonding Theory for Metals and Alloys*, 2nd ed.; Wang, F.E., Ed.; Elsevier: Amsterdam, The Netherlands, 2019; pp. 5–41. [CrossRef]
222. Springer, H.; Kostka, A.; Santos, J.F.D.; Raabe, D. Influence of intermetallic phases and Kirkendall-porosity on the mechanical properties of joints between steel and aluminium alloys. *Mater. Sci. Eng. A* **2011**, *528*, 4630–4642. [CrossRef]
223. Bergh, T.; Arbo, S.; Hagen, A.; Blindheim, J.; Friis, J.; Khalid, M.; Ringdalen, I.; Holmestad, R.; Westermann, I.; Vullum, P. On intermetallic phases formed during interdiffusion between aluminium alloys and stainless steel. *Intermetallics* **2022**, *142*, 107443. [CrossRef]
224. Chen, N.; Wang, M.; Wang, H.-P.; Wan, Z.; Carlson, B.E. Microstructural and mechanical evolution of Al/steel interface with Fe2Al5 growth in resistance spot welding of aluminum to steel. *J. Manuf. Process* **2018**, *34*, 424–434. [CrossRef]
225. Borrisutthekul, R.; Yachi, T.; Miyashita, Y.; Mutoh, Y. Suppression of intermetallic reaction layer formation by controlling heat flow in dissimilar joining of steel and aluminum alloy. *Mater. Sci. Eng. A* **2007**, *467*, 108–113. [CrossRef]
226. Hatano, R.; Ogura, T.; Matsuda, T.; Sano, T.; Hirose, A. Relationship between intermetallic compound layer thickness with deviation and interfacial strength for dissimilar joints of aluminum alloy and stainless steel. *Mater. Sci. Eng. A* **2018**, *735*, 361–366. [CrossRef]
227. Massalski, T.B.; Murray, J.L.; Bennett, L.H.; Baker, H. *Binary Alloy Phase Diagrams*; American Society for Metals: Metals Park, OH, USA, 1986.
228. Werner, M.R.; Fahrner, W.R. Review on Materials, Microsensors, Systems, and Devices for High-Temperature and Harsh-Environment Applications. *IEEE Trans. Ind. Electron.* **2001**, *48*, 249–257. [CrossRef]
229. Toropova, M. Bimaterial Lattices with Anisotropic Thermal Expansion. *J. Mech. Mater. Struct.* **2014**, *9*, 227–244. [CrossRef]
230. Yamamoto, N.; Gdoutos, E.; Toda, R.; White, V.; Manohara, H.; Daraio, C. Thin films with ultra-low thermal expansion. *Adv. Mater.* **2014**, *26*, 3076–3080. [CrossRef]
231. Zweben, C. Advances in composite materials for thermal management in electronic packaging. *JOM* **1998**, *50*, 47–51. [CrossRef]
232. Lu, D.D.; Wong, C.P. *Materials for Advanced Packaging*; Springer: New York, NY, USA, 2009. [CrossRef]
233. Bartnitzek, T.; Thelemann, T.; Apel, S.; Suphan, K.-H. Advantages and Limitations of Ceramic Packaging Technologies in Harsh Applications. 2016. Available online: http://meridian.allenpress.com/ism/article-pdf/2016/1/000581/2253545/isom-2016-thp23.pdf (accessed on 10 November 2023).
234. Ju, H.; Liu, S. Damage Degree analysis of storage failure modes for plastic encapsulated microelectronic devices. *J. Phys. Conf. Ser.* **2021**, *2132*, 12048. [CrossRef]
235. Wan, Y.J.; Li, G.; Yao, Y.M.; Zeng, X.L.; Zhu, P.L.; Sun, R. Recent advances in polymer-based electronic packaging materials. *Compos. Commun.* **2020**, *19*, 154–167. [CrossRef]
236. Lai, L.; Niu, B.; Bi, Y.; Li, Y.; Yang, Z. Advancements in SiC-Reinforced Metal Matrix Composites for High-Performance Electronic Packaging: A Review of Thermo-Mechanical Properties and Future Trends. *Micromachines* **2023**, *14*, 1491. [CrossRef]
237. Tong, X.C. Electronic Packaging Materials and Their Functions in Thermal Managements. In *Advanced Materials for Thermal Management of Electronic Packaging*; Springer Series in Advanced Microelectronics; Springer Science and Business Media Deutschland GmbH: Berlin/Heidelberg, Germany, 2011; Volume 30, pp. 131–167. [CrossRef]
238. Adachi, S. *Handbook on Physical Properties of Semiconductors*; Springer Science & Business Media: Berlin/Heidelberg, Germany, 2004.
239. Gale, W.F.; Totemeier, T.C. (Eds.) 15—Elastic properties, damping capacity and shape memory alloys. In *Smithells Metals Reference Book*, 8th ed.; Butterworth-Heinemann: Oxford, UK, 2004; pp. 1–45. [CrossRef]
240. Gale, W.F.; Totemeier, T.C. (Eds.) 14—General physical properties. In *Smithells Metals Reference Book*, 8th ed.; Butterworth-Heinemann: Oxford, UK, 2004; pp. 1–45. [CrossRef]
241. Kim, J.C.; Ren, Z.; Yuksel, A.; Dede, E.M.; Bandaru, P.R.; Oh, D.; Lee, J. Recent Advances in Thermal Metamaterials and Their Future Applications for Electronics Packaging. *J. Electron. Packag. Trans. ASME* **2021**, *143*, 10801. [CrossRef]
242. Vemuri, K.P.; Bandaru, P.R. An approach towards a perfect thermal diffuser. *Sci. Rep.* **2016**, *6*, 29649. [CrossRef]
243. Narayana, S.; Sato, Y. Heat Flux Manipulation with Engineered Thermal Materials. *Phys. Rev. Lett.* **2012**, *108*, 214303. [CrossRef]
244. Park, G.; Kang, S.; Lee, H.; Choi, W. Tunable multifunctional thermal metamaterials: Manipulation of local heat flux via assembly of unit-cell thermal shifters. *Sci. Rep.* **2017**, *7*, srep41000. [CrossRef] [PubMed]
245. Singhal, S.C. Solid oxide fuel cells for power generation. *WIREs Energy Environ.* **2014**, *3*, 179–194. [CrossRef]
246. Wee, J.H. Applications of proton exchange membrane fuel cell systems. *Renew. Sustain. Energy Rev.* **2007**, *11*, 1720–1738. [CrossRef]
247. Ferriday, T.B.; Middleton, P.H. Alkaline fuel cell technology—A review. *Int. J. Hydrogen Energy* **2021**, *46*, 18489–18510. [CrossRef]
248. Sammes, N.; Bove, R.; Stahl, K. Phosphoric acid fuel cells: Fundamentals and applications. *Curr. Opin. Solid State Mater. Sci.* **2004**, *8*, 372–378. [CrossRef]
249. Contreras, R.R.; Almarza, J.; Rincón, L. Molten carbonate fuel cells: A technological perspective and review. In *Energy Sources, Part A Recovery, Utilization and Environmental Effects*; Taylor and Francis Ltd.: Abingdon, UK, 2021. [CrossRef]

250. Hussain, S.; Yangping, L. Review of solid oxide fuel cell materials: Cathode, anode, and electrolyte. *Energy Transit.* **2020**, *4*, 113–126. [CrossRef]
251. Golkhatmi, S.Z.; Asghar, M.I.; Lund, P.D. A review on solid oxide fuel cell durability: Latest progress, mechanisms, and study tools. *Renew. Sustain. Energy Rev.* **2022**, *161*, 112339. [CrossRef]
252. Vishwanathan, A.S. Microbial fuel cells: A comprehensive review for beginners. *3 Biotech* **2021**, *11*, 248. [CrossRef]
253. Choudhury, A.; Chandra, H.; Arora, A. Application of solid oxide fuel cell technology for power generation—A review. *Renew. Sustain. Energy Rev.* **2013**, *20*, 430–442. [CrossRef]
254. Minh, N.Q.; Takahashi, T. Chapter 6—Anode. In *Science and Technology of Ceramic Fuel Cells*; Minh, N.Q., Takahashi, T., Eds.; Elsevier Science Ltd: Oxford, UK, 1995; pp. 147–164. [CrossRef]
255. Minh, N.Q.; Takahashi, T. Chapter 5—Cathode. In *Science and Technology of Ceramic Fuel Cells*; Minh, N.Q., Takahashi, T., Eds.; Elsevier Science Ltd: Oxford, UK, 1995; pp. 117–146. [CrossRef]
256. Wu, J.; Liu, X. Recent Development of SOFC Metallic Interconnect. *J. Mater. Sci. Technol.* **2010**, *26*, 293–305. [CrossRef]
257. Sakai, N.; Stølen, S. Heat capacity and thermodynamic properties of lanthanum(III) chromate(III): $LaCrO_3$, at temperatures from 298.15 K. Evaluation of the thermal conductivity. *J. Chem. Thermodyn.* **1995**, *27*, 493–506. [CrossRef]
258. Jiang, W.; Zhang, Y.; Woo, W.; Tu, S.T. Three-dimensional simulation to study the influence of foil thickness on residual stress in the bonded compliant seal design of planar solid oxide fuel cell. *J. Power Sources* **2012**, *209*, 65–71. [CrossRef]
259. Marina, O.A.; Canfield, N.L.; Stevenson, J.W. Thermal, electrical, and electrocatalytical properties of lanthanum-doped strontium titanate. *Solid State Ion.* **2002**, *149*, 21–28. [CrossRef]
260. Ullmann, H.; Trofimenko, N.; Tietz, F.; Stöver, D.; Ahmad-Khanlou, A. Correlation between thermal expansion and oxide ion transport in mixed conducting perovskite-type oxides for SOFC cathodes. *Solid State Ion.* **2000**, *138*, 79–90. [CrossRef]
261. Abdin, Z.; Khalilpour, K.R. Chapter 4—Single and Polystorage Technologies for Renewable-Based Hybrid Energy Systems. In *Polygeneration with Polystorage for Chemical and Energy Hubs*; Khalilpour, K.R., Ed.; Academic Press: Cambridge, MA, USA, 2019; pp. 77–131. [CrossRef]
262. Petric, A.; Huang, P.; Tietz, F. Evaluation of La–Sr–Co–Fe–O perovskites for solid oxide fuel cells and gas separation membranes. *Solid State Ion.* **2000**, *135*, 719–725. [CrossRef]
263. Ni, Q.; Chen, H.; Ge, L.; Yu, S.; Guo, L. Investigation of La1−xSmx−ySryCoO3−δ cathode for intermediate temperature solid oxide fuel cells. *J. Power Sources* **2017**, *349*, 130–137. [CrossRef]
264. Hayun, H.; Wolf, R.; Barad, C.; Gelbstein, Y. Thermal shock resistant solid oxide fuel cell ceramic composite electrolytes. *J. Alloys Compd.* **2020**, *821*, 153490. [CrossRef]
265. Zhang, Y.; Chen, B.; Guan, D.; Xu, M.; Ran, R.; Ni, M.; Zhou, W.; O'Hayre, R.; Shao, Z. Thermal-expansion offset for high-performance fuel cell cathodes. *Nature* **2021**, *591*, 246–251. [CrossRef]
266. Zhou, W.; Shao, Z.; Ran, R.; Cai, R. Novel $SrSc_{0\cdot 2}Co_{0\cdot 8}O_3$-δ as a cathode material for low temperature solid-oxide fuel cell. *Electrochem. Commun.* **2008**, *10*, 1647–1651. [CrossRef]
267. Zhou, W.; Ran, R.; Shao, Z.; Jin, W.; Xu, N. Evaluation of A-site cation-deficient $(Ba_{0\cdot 5}Sr_{0\cdot 5})_{1\text{-}x}Co_{0\cdot 8}Fe_{0\cdot 2}O_3$-δ (x > 0) perovskite as a solid-oxide fuel cell cathode. *J. Power Sources* **2008**, *182*, 24–31. [CrossRef]
268. Ding, X.; Cui, C.; Guo, L. Thermal expansion and electrochemical performance of $La_{0.7}Sr_{0.3}CuO_{3\text{-}\delta}$-$Sm_{0.2}Ce_{0.8}O_{2\text{-}\delta}$ composite cathode for IT-SOFCs. *J. Alloys Compd.* **2009**, *481*, 845–850. [CrossRef]
269. Song, Y.; Chen, Y.; Xu, M.; Wang, W.; Zhang, Y.; Yang, G.; Ran, R.; Zhou, W.; Shao, Z. A Cobalt-Free Multi-Phase Nanocomposite as Near-Ideal Cathode of Intermediate-Temperature Solid Oxide Fuel Cells Developed by Smart Self-Assembly. *Adv. Mater.* **2020**, *32*, e1906979. [CrossRef] [PubMed]
270. Jia, X.; Lu, F.; Liu, K.; Han, M.; Su, J.; He, H.; Cai, B. Improved performance of IT-SOFC by negative thermal expansion $Sm_{0\cdot 85}Zn_{0\cdot 15}MnO_3$ addition in $Ba_{0\cdot 5}Sr_{0\cdot 5}Fe_{0\cdot 8}Cu_{0\cdot 1}Ti_{0\cdot 1}O_3$-δcathode. *J. Phys. Cond. Matter* **2022**, *34*, 184001. [CrossRef]
271. Minh, N.Q. Ceramic Fuel Cells. *J. Am. Ceram. Soc.* **1993**, *76*, 563–588. [CrossRef]
272. Fergus, J.W. Metallic interconnects for solid oxide fuel cells. *Mater. Sci. Eng. A* **2005**, *397*, 271–283. [CrossRef]
273. Hodjati-Pugh, O.; Dhir, A.; Steinberger-Wilckens, R. The development of current collection in micro-tubular solid oxide fuel cells—A review. *Appl. Sci.* **2021**, *11*, 1077. [CrossRef]
274. Niewolak, L.; Tietz, F.; Quadakkers, W.J. Interconnects. In *High-Temperature Solid Oxide Fuel Cells for the 21st Century: Fundamentals, Design and Applications*; Elsevier: Amsterdam, The Netherlands, 2015; pp. 195–254. [CrossRef]
275. Horita, T.; Xiong, Y.; Kishimoto, H.; Yamaji, K.; Brito, M.E.; Yokokawa, H. Chromium Poisoning and Degradation at $(La,Sr)MnO_3$ and $(La,Sr)FeO_3$ Cathodes for Solid Oxide Fuel Cells. *J. Electrochem. Soc.* **2010**, *157*, B614. [CrossRef]
276. Yang, Z.; Weil, K.S.; Paxton, D.M.; Stevenson, J.W. Selection and Evaluation of Heat-Resistant Alloys for SOFC Interconnect Applications. *J. Electrochem. Soc.* **2003**, *150*, A1188. [CrossRef]
277. Kofstad, P.; Bredesen, R. High temperature corrosion in SOFC environments. *Solid State Ion.* **1992**, *52*, 69–75. [CrossRef]
278. Yang, Z.; Xia, G.G.; Stevenson, J.W. Evaluation of Ni-Cr-base alloys for SOFC interconnect applications. *J. Power Sources* **2006**, *160*, 1104–1110. [CrossRef]
279. Zohrabian, V.M.; Sonick, M.; Hwang, D.; Abrahams, J.J. Dental Implants. *Semin. Ultrasound CT MRI* **2015**, *36*, 415–426. [CrossRef]
280. Hao, C.P.; Cao, N.J.; Zhu, Y.H.; Wang, W. The osseointegration and stability of dental implants with different surface treatments in animal models: A network meta-analysis. *Sci. Rep.* **2021**, *11*, 13849. [CrossRef]

281. Panchal, M.; Khare, S.; Khamkar, P.; Bhole, K.S. Dental implants: A review of types, design analysis, materials, additive manufacturing methods, and future scope. *Mater. Today Proc.* **2022**, *68*, 1860–1867. [CrossRef]
282. Nicholson, J.W. Titanium Alloys for Dental Implants: A Review. *Prosthesis* **2020**, *2*, 100–116. [CrossRef]
283. Prathapachandran, J.; Suresh, N. Management of peri-implantitis. *Dent. Res. J.* **2012**, *9*, 516.
284. Noyama, Y.; Miura, T.; Ishimoto, T.; Itaya, T.; Niinomi, M.; Nakano, T. Bone loss and reduced bone quality of the human femur after total hip arthroplasty under stress-shielding effects by titanium-based implant. *Mater. Trans.* **2012**, *53*, 565–570. [CrossRef]
285. Niu, L.; Dong, S.J.; Kong, T.T.; Wang, R.; Zou, R.; Da Liu, Q. Heat transfer behavior across the dentino-enamel junction in the human tooth. *PLoS ONE* **2016**, *11*, e0158233. [CrossRef]
286. Jacobs, H.R.; Thompson, R.E.; Brown, W.S. Heat Transfer in Teeth. *J. Dent. Res.* **1973**, *52*, 248–252. [CrossRef]
287. Li, S.; Chien, S.; Brånemark, P.I. Heat shock-induced necrosis and apoptosis in osteoblasts. *J. Orthop. Res.* **1999**, *17*, 891–899. [CrossRef]
288. Eriksson, A.R.; Albrektsson, T. Temperature threshold levels for heat-induced bone tissue injury: A vital-microscopic study in the rabbit. *J. Prosthet. Dent.* **1983**, *50*, 101–107. [CrossRef]
289. Ormianer, Z.; Feuerstein, O.; Assad, R.; Samet, N.; Weiss, E.I. In vivo changes in dental implant temperatures during hot beverage intake: A pilot study. *Implant Dent.* **2009**, *18*, 38–45. [CrossRef]
290. Froes, F.; Gungor, M.N.; Imam, M.A. Overview Titanium's Expanding Market Cost-Affordable Titanium: The Component Fabrication Perspective. *JOM* **2007**, *59*, 28–31. [CrossRef]
291. Anderson, B.J.; Justus, C.G.; Batts, G.W. Guidelines for the Selection of Near-Earth Thermal Environment Parameters for Spacecraft Design. 2001. Available online: http://www.sti.nasa.gov (accessed on 15 November 2023).
292. Ghidini, T. Materials for space exploration and settlement. *Nat. Mater.* **2018**, *17*, 846–850. [CrossRef] [PubMed]
293. Lu, G.Y.; Zhou, J.Y.; Cai, G.P.; Fang, G.Q.; Lv, L.L.; Peng, F.J. Studies of thermal deformation and shape control of a space planar phased array antenna. *Aerosp. Sci. Technol.* **2019**, *93*, 105311. [CrossRef]
294. Bhundiya, H.G.; Royer, F.; Cordero, Z. Engineering Framework for Assessing Materials and Processes for In-Space Manufacturing. *J. Mater. Eng. Perform.* **2022**, *31*, 6045–6059. [CrossRef]
295. Yu, B.; Xu, Z.; Mu, R.; Wang, A.; Zhao, H. Design of Large-Scale Space Lattice Structure with Near-Zero Thermal Expansion Metamaterials. *Aerospace* **2023**, *10*, 294. [CrossRef]
296. Milward, S.S. Controlling Thermal Expansion with Lattice Structures Using Laser Powder Bed Fusion Laser Powder Bed Fusion Process Development. 2017. Available online: http://www.swansea.ac.uk/library/researchsupport/ris-support/ (accessed on 18 November 2023).

Disclaimer/Publisher's Note: The statements, opinions and data contained in all publications are solely those of the individual author(s) and contributor(s) and not of MDPI and/or the editor(s). MDPI and/or the editor(s) disclaim responsibility for any injury to people or property resulting from any ideas, methods, instructions or products referred to in the content.